The evolution of the cold interstellar medium in galaxies following a starburst

K. Rowlands, V. Wild, N. Nesvadba, B. Sibthorpe, A. Mortier, M. Lehnert, E. da Cunha

HAL Id: insu-03644739
https://insu.hal.science/insu-03644739

Submitted on 25 Apr 2022

The evolution of the cold interstellar medium in galaxies following a starburst[*]

K. Rowlands,[1][†] V. Wild,[1] N. Nesvadba,[2] B. Sibthorpe,[3] A. Mortier,[4] M. Lehnert[5] and E. da Cunha[6]

[1]*(SUPA) School of Physics & Astronomy, University of St Andrews, North Haugh, St Andrews, Fife KY16 9SS, UK*
[2]*Institut d'Astrophysique Spatiale, CNRS, Université Paris-Sud, Bat. 120-121, F-91405 Orsay, France*
[3]*SRON Netherlands Institute for Space Research, Zernike Building, PO Box 800, NL-9700 AV Groningen, the Netherlands*
[4]*School of Physics & Astronomy, The University of Nottingham, University Park Campus, Nottingham NG7 2RD, UK*
[5]*Institut d'Astrophysique de Paris, UMR 7095, CNRS, Université Pierre et Marie Curie, 98 bis boulevard Arago, F-75014 Paris, France*
[6]*Max Planck Institute for Astronomy, Konigstuhl 17, D-69117 Heidelberg, Germany*

ABSTRACT

We present the evolution of dust and molecular gas properties in a sample of 11 $z \sim 0.03$ starburst to post-starburst (PSB) galaxies selected to span an age sequence from ongoing starburst to 1 Gyr after the starburst ended. All PSBs harbour significant molecular gas and dust reservoirs and residual star formation, indicating that complete quenching of the starburst due to exhaustion or expulsion of gas has not occurred during this timespan. As the starburst ages, we observe a clear decrease in the star formation efficiency, molecular gas and star formation rate (SFR) surface density, and effective dust temperature, from levels coincident with starburst galaxies to those of normal star-forming galaxies. These trends are consistent with a natural decrease in the SFR following consumption of molecular gas by the starburst, and corresponding decrease in the interstellar radiation field strength as the starburst ages. The gas and dust contents of the PSBs are coincident with those of star-forming galaxies and molecular gas-rich early-type galaxies, and are not consistent with galaxies on the red sequence. We find no evidence that the global gas reservoir is expelled by stellar winds or active galactic nuclei feedback. Our results show that although a strong starburst in a low-redshift galaxy may cause the galaxy to ultimately have a lower specific SFR and be of an earlier morphological type, the galaxy will remain in the 'green valley' for an extended time. Multiple such episodes may be needed to complete migration of the galaxy from the blue- to red sequence.

Key words: dust, extinction – galaxies: evolution – galaxies: interactions – galaxies: ISM – galaxies: starburst – submillimetre: galaxies.

1 INTRODUCTION

It has long been known that the galaxy population displays a colour bimodality (Strateva et al. 2001; Blanton et al. 2003; Baldry et al. 2004; Bell et al. 2004). The dearth of green valley galaxies relative to the optically blue and red populations, together with the gradual build-up of mass on the red sequence over cosmic time, has led to the idea that many galaxies must undergo a rapid change in colour due to quenching of star formation on a $\lesssim 1$ Gyr time-scale (Kaviraj et al. 2007; Martin et al. 2007; Schawinski et al. 2007; Wild et al. 2009; Yesuf et al. 2014).

Post-starburst (PSB) galaxies are candidates for such a transition population. These galaxies have undergone a starburst in the recent ($\lesssim 1$ Gyr) past which has since declined rapidly in strength, leaving a dominant A/F-star population. Local PSBs which have completely quenched their star formation are found to have predominantly early-type morphologies (Wong et al. 2012; Mendel et al. 2013), and a large fraction exhibit morphological disturbances (Zabludoff et al. 1996; Blake et al. 2004; Goto 2005; Yang et al. 2008; Pracy et al. 2009; Pawlik et al., in preparation). This has led to the hypothesis that the starburst was triggered by a merger or interaction, at least in the local Universe where gas-to-stellar mass ratios of massive galaxies are relatively low (Bekki, Shioya & Couch 2001; Bekki et al. 2005; Snyder et al. 2011, but see Dressler et al. 2013 for

an alternative view). Simulations show how an interaction may funnel gas towards the centre of the galaxy (e.g. Mihos & Hernquist 1994, 1996; Barnes & Hernquist 1996), leading to an increase in gas density and subsequent strong star formation, ultimately consuming the entire gas reservoir.

While the number density of PSB galaxies at $z \gtrsim 1$ indicates that they could represent a significant channel for red-sequence growth (Wild et al. 2009; Whitaker et al. 2012a; Yesuf et al. 2014), the true global importance of PSB galaxies for the wider picture of galaxy evolution depends on whether the quenching of star formation is permanent or temporary.

To reach the red sequence, the gas reservoir in galaxies must be exhausted, and/or prevented from forming stars via feedback mechanisms (e.g. Benson et al. 2003; Di Matteo, Springel & Hernquist 2005). Using simple energetics arguments, Kaviraj et al. (2007) suggested that supernova (SN) feedback is consistent with being the dominant quenching mechanism of star formation in nearby low stellar mass ($M_* < 10^{10}$ M$_\odot$) PSBs, and feedback from active galactic nuclei (AGN) dominates in high-mass ($M_* > 10^{10}$ M$_\odot$) PSBs (see also Wong et al. 2012). Smoothed particle hydrodynamic simulations of merging galaxies routinely show how the starburst initially declines through the depletion of gas supplies, but additional energy must be injected into the interstellar medium (ISM) to completely quench star formation throughout the entire galaxy. Energy input from an AGN is usually invoked to complete the transition of galaxies from blue to red sequence, through gas heating or expulsion (e.g. Springel, Di Matteo & Hernquist 2005; Hopkins et al. 2007; Khalatyan et al. 2008; Kaviraj et al. 2011). However, there remains no direct observational evidence for such a scenario (although see Alatalo et al. 2014).

Due to the rarity of PSBs in the local Universe, they are not routinely included in large neutral and molecular gas surveys. Without the need for selection with moderate signal-to-noise optical spectroscopy, close pair/pre-merger samples and IR bright starburst/coalescence phases have been better studied with targeted observations (e.g. Sanders, Scoville & Soifer 1991; Braine & Combes 1993; Solomon et al. 1997; Casasola, Bettoni & Galletta 2004; Boquien et al. 2011b; García-Burillo et al. 2012). Recently, Zwaan et al. (2013) detected H I gas in 6/11 galaxies with PSB populations at $z \sim 0.03$, finding that they have atomic gas-to-stellar mass ratios between those of early-type galaxies (ETGs) and spirals. Although these results show that local PSBs may not have run out of gas entirely, H I is not directly connected to star formation as it dominates the ISM when gas surface densities are <10 M$_\odot$ pc^{-2} (Bigiel et al. 2008). Knowledge of their molecular gas contents is required to ascertain why galaxies have stopped forming stars. It is also advantageous to study PSBs with a range of ages, and in conjunction with samples of starbursts from which they originated, so we can track how the state of the ISM alters as the impact of the starburst decays. This has not been the case in previous studies, where stringent limits placed on nebula emission line strengths ensures that all star formation has completely ceased and therefore only the oldest PSBs (and those without type-II AGN) are selected for follow-up.

In this paper, we examine the cold gas and dust properties of a sample of starbursts and PSBs at $z \sim 0.03$ with a range of ages from 0 to 1 Gyr after the starburst, selected from the spectroscopic sample of the Sloan Digital Sky Survey (SDSS) Data Release 7 (DR7; Abazajian et al. 2009). We focus purely on galaxies with significant bulges (selected with high stellar surface mass density, μ*) where the star formation processes are more extreme than in disc-dominated systems (Kennicutt 1998, hereafter K98), and the majority of accretion on to black holes occurs (Kauffmann et al. 2003b). The sample

is selected purely based on the properties of the stellar population of the galaxies, i.e. with no cut on nebular emission line strength. This serves two purposes: (1) it does not bias against objects containing obscured (narrow line) AGN which may be more prevalent in PSBs than other phases of galaxy evolution (Yan et al. 2006; Georgakakis et al. 2008; Brown et al. 2009; Yesuf et al. 2014), and (2) allows us to select PSBs with a range of ages, as starbursts are not instantaneous, but rather decay over ~100 Myr time-scales meaning nebular emission lines are expected to be present even during the PSB phase (Yan et al. 2006; Falkenberg, Kotulla & Fritze 2009; Snyder et al. 2011). By selecting purely based on known physical properties of the stellar population, (i.e. starburst age and burst strength), we can select a complete sample of objects in a physically meaningful sense. In Section 2, we describe the method used to select a complete sample of starburst to PSB galaxies. In Section 3, we describe the multiwavelength data obtained for this study and our spectral energy distribution (SED) fitting method. The results are presented in Section 4 and our conclusions in Section 5. We adopt a cosmology with $\Omega_m = 0.30$, $\Omega_\Lambda = 0.70$ and $H_0 = 70$ km s^{-1} Mpc^{-1}.

2 SAMPLE SELECTION

In the integrated optical fibre spectrum of a galaxy, the different signatures of stars of different ages can be used to obtain information about a galaxy's recent star formation history (SFH). To define our sample, we make use of two particular features of optical spectra: the 4000 Å break strength and Balmer absorption line strength. In Fig. 1, we show the distribution of two spectral indices which parametrize these features for 70 000 bulge-dominated galaxies with stellar surface mass density $\mu^* = M_*/(2\pi r_{50,z}^2) > 3 \times 10^8$ M$_\odot$ kpc^{-2} at $0.01 < z < 0.07$ in the SDSS. These two spectral indices are based on a principal component analysis (PCA) of the 3175–4150 Å
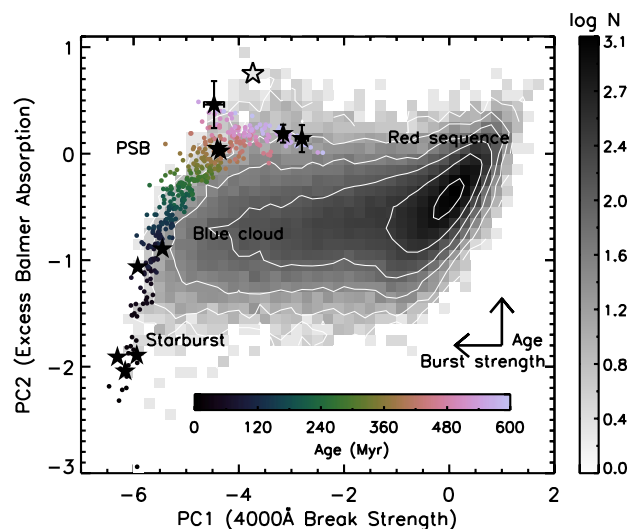

Figure 1. The 4000 Å break strength and Balmer absorption line strength as measured by a principal component analysis of the 4000 Å spectral region of the targeted galaxies (stars). The grey-scale indicates the distribution of all SDSS DR7 galaxies with spectral per-pixel-SNR >8 in the g-band, redshift $0.01 < z < 0.07$ and stellar surface mass densities $>3 \times 10^8$ M$_\odot$ kpc^{-2}. The coloured dots indicate the (post-)starburst sample from which the targets were selected. The open star indicates the position of the additional target 'PSB11', an older PSB galaxy than the completeness limit of the original starburst sample. Errors are indicated only where they are significantly larger than the symbol size.

region of the spectra, and describe the strength of the 4000 Å break, and excess Balmer absorption over that expected for the 4000 Å break strength (Wild et al. 2007). As expected for bulge-dominated galaxies, the majority of the galaxies show no evidence of recent or current star formation, they form the 'red sequence' which lies on the right, with strong 4000 Å break strength from the old stars. Galaxies that are forming stars have younger mean stellar ages and therefore weaker 4000 Å break strengths and form the 'blue sequence'. A small number of galaxies are undergoing a 'starburst', i.e. there has been a sharp increase in the galaxy's star formation rate (SFR) over a short time-scale ($\sim 10^7$ yr). These galaxies are identified by their unusually weak Balmer absorption lines, strong UV–blue continua and weak 4000 Å breaks, i.e. spectra dominated by light from O/B stars. These objects lie in the lower left of Fig. 1. As the starburst ages to a few 10^8 yr, the Balmer absorption lines increase in strength as the galaxy passes into the PSB phase (Dressler & Gunn 1983; Couch & Sharples 1987), i.e. A/F star light dominates the integrated galaxy spectrum. These objects lie in the upper left of Fig. 1. A comparison of our selection technique to the classical definition of PSB galaxies (e.g. lack of Hα, [O II] and deep Balmer absorption) is presented in Appendix A.

2.1 Measuring starburst age

The rapidly changing appearance of the galaxy optical spectrum during and following a starburst, together with the enhanced luminosity of young stars compared to the old (non-starburst) population, allows the robust measurement of starburst age. A full Bayesian spectral synthesis model analysis of the optical spectra, allowing for variations in dust attenuation and previous SFH, yields uncertainties of the order of 20 Myr for the youngest objects to 100 Myr as the starburst ages to ~ 1 Gyr (Wild, Heckman & Charlot 2010). Unfortunately, burst strength at a given starburst age is less well constrained for individual objects, and is more dependent on the underlying SFH of the galaxy. At ages older than ~ 600 Myr, a degeneracy becomes apparent between burst age and mass, leading Wild et al. (2010) to restrict their evolutionary sequence to ages younger than this.

Through comparison with population synthesis models, using simple toy model SFHs or more complex histories derived from simulations, Wild et al. (2007, 2009) showed that the shape of the left-hand side of the distribution in Fig. 1 describes the evolutionary track of a starburst galaxy, with time since the starburst increasing from bottom to top, and burst strength increasing from right to left. The galaxies lying at the outermost edge of the distribution have undergone the strongest recent bursts of star formation in the entire sample. At these low redshifts, these starbursts are not strong; Bayesian fits to spectral synthesis models imply typical burst mass fractions (i.e. fraction of stellar mass formed in the burst) of ~ 10 per cent. The models show that if galaxies that had undergone stronger bursts existed, they would lie to the left of the distribution at intermediate starburst ages, where no galaxies are observed. Thus, the visualization of the full distribution of objects, rather than fits to individual objects, allows us to better constrain the parameters of the population as a whole.

The coloured dots in Fig. 1 are selected to form a complete (constant number per unit starburst age) sample of the 400 strongest starbursts in SDSS galaxies with high μ^*. The definition of this sample is discussed in greater detail in Wild et al. (2010, hereafter WHC10). Briefly, a Bayesian fit was performed to the PCA indices of the individual galaxies to determine starburst age (t_{SB}) using

a set of 10^7 spectral synthesis models with SFHs composed of an old bulge population with superposed exponentially decaying starbursts. Burst mass fraction, burst age, decay rate and dust content were free to vary with uniform priors. The resulting errors on the starburst age therefore take into account the potential variations in recent SFH and dust content of the galaxies and account for possible degeneracies between model parameters.

2.2 Sample for follow-up millimetre and far-infrared observations

From this base sample of galaxies which have undergone the strongest recent bursts of star formation in the local Universe, we selected 11 targets for follow-up carbon monoxide (CO) and far-infrared (FIR) observations, indicated as stars in Fig. 1.

(i) We targeted four starburst ages (t_{SB}), either side of the observed discontinuities in L(Hα) (see Section 3.1): three galaxies with $t_{SB} < 50$ Myr, two with $t_{SB} \sim 100$ Myr, two with $t_{SB} \sim 400$ Myr and three with $t_{SB} \sim 600$ Myr. To extend the time baseline probed by our observations, we additionally targeted an older PSB galaxy, which is too old to form part of the complete sample described above (open star in Fig. 1). As discussed above, typical errors on t_{SB} are significantly less than the difference in ages between the bins.

(ii) All objects have typical Hα luminosities for their starburst age (see Section 3.1).

(iii) We ensured that galaxies in each of the four samples have similar stellar mass[1] ($9.6 < \log_{10}(M_*/M_\odot) < 10.4$) and redshift ($0.025 < z < 0.05$).

Table 1 gives the name, position, SDSS spectroscopic ID and redshift of all targets. The final column gives the integration time for the CO observations (Section 3.2).

The r-band half-light radius (Petrosian R_{50}) of the sample ranges from 1.5–5.2 arcsec (1.0–3.4 kpc in physical radius). It is important to note that our sample has been selected primarily on properties derived from spectra which probe the central 3 arcsec of the galaxies (0.9–1.4 kpc in physical radius), which extends from 0.3–1.0 times the half-light radius. We take care to note this where relevant to our results.

Fig. 2 shows how the central SFR (measured from dust-corrected Hα luminosity within the 3 arcsec SDSS fibre) declines with starburst age as derived from the stellar continuum. Overall, we measure a decline time-scale of ~ 300 Myr similar to that expected from disc dynamical time-scales (Lehnert & Heckman 1996). However, we clearly identify three phases: a short 'starburst' phase of the order of 10–30 Myr, an almost flat 'coasting' phase which lasts to around 400 Myr, and a subsequent decline. It is clear, even from the SDSS data, that star formation has not shut down instantaneously following the starburst, and residual star formation continues long into the PSB phase. The aim of the CO and FIR observations presented in this paper is to study the galaxy-wide reservoir of molecular gas that is fuelling this ongoing star formation.

---

[1] During selection, the stellar mass was measured using a Bayesian fit of stellar population synthesis models to the five-band SDSS photometry (J. Brinchmann; http://www.mpa-garching.mpg.de/SDSS).

Table 1. Object name, position, SDSS DR7 specobjid, optical redshift and total on-source integration time for the millimetre observations.

Object ID	RA (J2000 deg)	Dec (J2000 deg)	Specobjid	z	t_{int} (min)
PSB1	233.132	57.8829	173331940055711744	0.039	570 (600)[a]
PSB2	228.951	20.0224	607094233467191296	0.036	240
PSB3	225.401	16.7297	782453208889950208	0.032	300
PSB4	246.455	40.3452	330115272746729472	0.029	240
PSB5	244.398	14.0523	711521640860614656	0.034	240
PSB6	252.924	41.6684	177834388912865280	0.043	120
PSB7	249.495	13.8594	622289631202770944	0.047	240
PSB8	232.702	55.3288	173055146299752448	0.046	420
PSB9	239.568	52.4893	174175084368363520	0.049	480
PSB10	247.179	22.3971	442707057922015232	0.034	480
PSB11	237.803	14.6964	709269844574339072	0.048	360

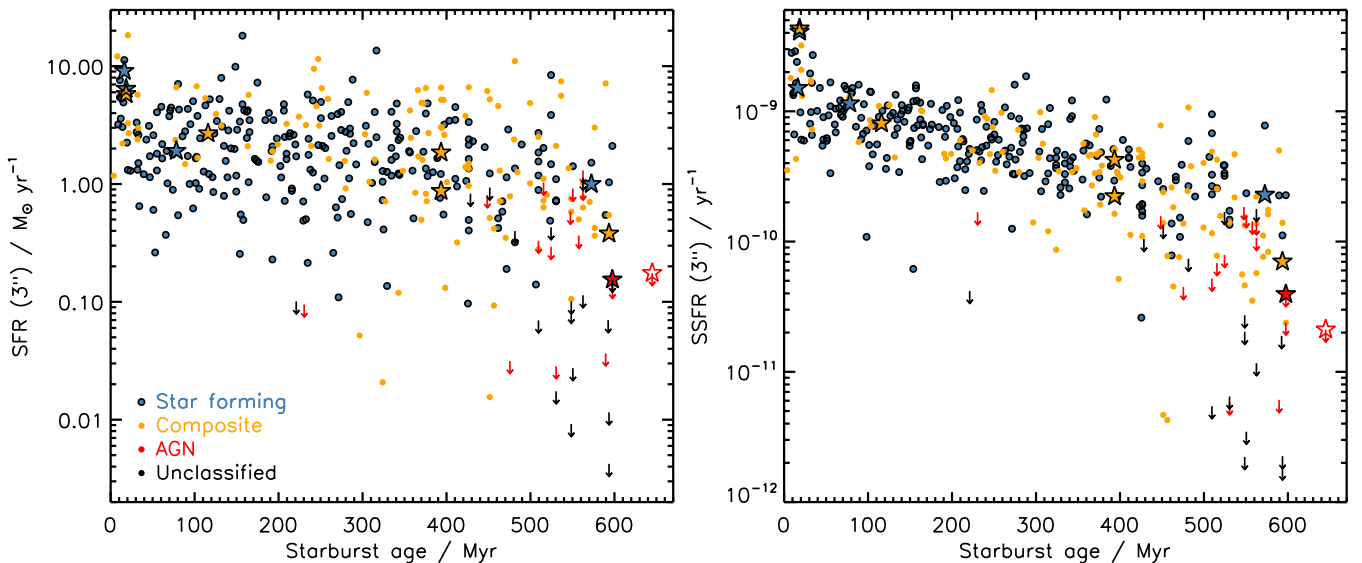*Note.* [a]Combined spectra contain 38 scans at CO(1–0) and 40 scans at CO(2–1).

Figure 2. The SFR (SFR, left-hand panel) and specific SFR (SSFR = SFR/M_*, right-hand panel) within the 3 arcsec SDSS fibre of the targeted galaxies (stars) and full starburst sample (dots), as a function of time since the starburst. Galaxies are classified as star forming (blue), composites (orange) or AGN (red) on the BPT diagram (Baldwin, Phillips & Terlevich 1981; Veilleux & Osterbrock 1987). Composite galaxies have had the AGN contribution to their Hα luminosity removed, based on the correction presented in WHC10, before their SFR is calculated. A similar correction is not attempted for the AGN, and these are shown as upper limits based on their total Hα luminosity. 'PSB11' has a starburst age of ∼1 Gyr, and is indicated as an open star at the rightmost edge of each panel.

3 DATA AND METHODS

3.1 Optical data

The SDSS is an optical photometric and spectroscopic survey of local galaxies (York et al. 2000). The final data release of SDSS-II (DR7, Abazajian et al. 2009) includes 9380 deg^2 with spectroscopic coverage, targeting nearly 10^6 galaxies with Petrosian r-band magnitudes <17.77. The spectra have good signal to noise and moderate resolution which allows the deconvolution of stellar continuum from nebular emission that is crucial to accurately measure Balmer decrements. Such a deconvolution has been carried out by Brinchmann et al. (2004) and Tremonti et al. (2004) and the emission line measurements are available at http://www.mpa-garching.mpg.de/SDSS.

From the SDSS data, we extract the following information.

(i) Model magnitudes in the u, g, r, i and z bands as an input to the MAGPHYS SED fitting.[2]

(ii) Nebular emission line fluxes in the central 3 arcsec, corrected for underlying stellar continuum absorption, from Brinchmann et al. (2004) and Tremonti et al. (2004). These provide the Hα and Hβ line fluxes to estimate dust-corrected Hα luminosity, and allow detection of a possible AGN using the BPT diagram ([N II]/Hα and [O III]/Hβ emission line ratios; Baldwin et al. 1981; Veilleux & Osterbrock 1987).

(iii) Stellar continuum indices measured in the central 3 arcsec, PC1 and PC2, which measure the 4000 Å break strength

---

[2] To the u and z bands, we apply a small correction of -0.04 and $+0.02$ magnitudes, respectively, to bring them on to the AB magnitude calibration (http://classic.sdss.org/dr7/algorithms/fluxcal.html#sdss2ab).

Table 2. Physical parameters derived from SDSS data. Note that starburst age, stellar mass, SFR, metallicity and emission line class are measured within the central 3 arcsec (0.9–1.4 kpc in physical radius). Composite galaxies have had the AGN contribution to their Hα luminosity removed, based on the correction presented in WHC10, before their SFR is calculated. A similar correction is not attempted for the AGN, for which SFR is given as an upper limit based on their total Hα luminosity.

Name	σ^* (km s^{-1})	Starburst age (Myr)	$\log_{10}$(Stellar mass) (M$_\odot$)	$12+\log(O/H)^a$	SFR (M$_\odot$ yr^{-1})	Emission line class
PSB1	86 ± 13	18^{+4}_{-8}	9.8	8.9	$6.4^{+0.4}_{-0.4}$	SF
PSB2	131 ± 10	16^{+2}_{-6}	10.7	9.0	$9.1^{+0.4}_{-0.5}$	SF
PSB3	114 ± 10	18^{+1}_{-4}	9.6	9.0	~ 5.8	comp
PSB4	96 ± 12	78^{+15}_{-31}	10.4	8.8	$1.9^{+0.1}_{-0.2}$	SF
PSB5	88 ± 8	116^{+36}_{-65}	9.9	-99.9	~ 2.7	comp
PSB6	110 ± 7	394^{+38}_{-74}	10.4	-99.9	~ 1.8	comp
PSB7	76 ± 7	394^{+36}_{-63}	10.2	9.1	~ 0.9	comp
PSB8	96 ± 6	598^{+111}_{-82}	10.0	-99.9	<0.2	AGN
PSB9	87 ± 8	594^{+514}_{-12}	10.3	9.0	~ 0.4	comp
PSB10	93 ± 15	573^{+165}_{-57}	10.2	8.9	$1.0^{+0.1}_{-0.1}$	SF
PSB11	101 ± 6	996^{+55}_{-169}	10.5	-99.9	<0.2	AGN

Note. ^{a}Gas phase oxygen abundance from Tremonti et al. (2004), -99.9 where unmeasured for galaxies with AGN signatures. Note that due to a slightly less stringent demarcation between star-forming and composite galaxies used in Tremonti et al. (2004), some galaxies we class as 'composite' are classed as star forming in Tremonti et al. (2004) and therefore have a metallicity measurement.

and the Balmer absorption lines as described in Section 2 (Wild et al. 2007).

(iv) Stellar surface mass density (μ*) calculated as $M_*/(2\pi r_{50,z}^2)$ where $r_{50,z}$ is the physical size in kpc of the radius which contains 50 per cent of the z-band Petrosian flux.

In Table 2, we give the parameters derived from SDSS data that are most relevant to this paper for each object in our sample. The multicolour *gri* SDSS images of the target galaxies are shown in Appendix B1 with the size of the 3 arcsec SDSS fibre and the Institut de Radioastronomie Millimétrique (IRAM) beam size at 115 and 230 GHz. The images are ordered by starburst age indicated at the top of each panel. Visual inspection of the images reveals that galaxies with the youngest starbursts are generally extremely blue, with clear signs of recent disruption. The host galaxies of older starbursts are redder, with occasional signs of past disruption (see Pawlik et al. in preparation). For a larger selection of images of the oldest and youngest starbursts in the parent sample, see figs A1 and A2 in WHC10.

The SDSS spectra are shown in Fig. B2, over the full optical range in the right-hand column and zoomed in on the 4000 Å break region in the left-hand column. The PCA fits to the 4000 Å break region, from which the stellar indices PC1 and PC2 and in turn the starburst ages are measured, are overplotted in red. The emission line classification of each object is given in the right-hand panels, based upon their position on the BPT diagram. Galaxies that lie below the demarcation line of WHC10 are classified as star forming, those lying above the demarcation line of Kewley et al. (2001) are classified as AGN and those lying in between are classified as star-forming-AGN composites. We note that these classes are artificial: first, the lines are either empirically derived in the case of WHC10, or derived from theoretical models subsequently shown to be inaccurate (Levesque, Kewley & Larson 2010); and secondly the position of a galaxy in the diagram depends on the SFR relative to black hole accretion rate in the 3 arcsec SDSS fibre. However, they provide a useful first-order classification between objects where the nebular emission lines are dominated by star formation and therefore

only a weak AGN can exist, or those with a rapidly accreting AGN. It should be noted that pure AGN are not visible until the older PSB stage, due to the high SFRs at young ages. See WHC10 for more details.

3.2 CO data

We observed all objects on the nights of 2010 June 29/30 with the IRAM-30m telescope. The Eight MIxer Receiver (EMIR) was used in wobbler switching mode with reference positions offset by ±100 arcsec. We used the Wideband Line Multiple Autocorrelator (WILMA) backend with the standard instrument setup which allowed us to obtain simultaneous measurements of CO(1–0) at 3 mm and CO(2–1) at 1 mm, with a resolution of 2 MHz (∼5 kms^{-1} at the observing frequency). We also simultaneously recorded data at 3 mm with VErsatile SPectrometer Assembly (VESPA) and with the 4 MHz filterbank at 1 mm as a backup. In general, measurements from the different receivers are consistent within the 1σ errors. Conditions were generally good, with only 2 h lost due to rain or excessive cloud. The precipitable water vapour at 3 mm ranged from 4.7–37.8 mm, with a mean of 13.9 mm. The total on-source integration time in minutes is shown in Table 1.

Scans of 6 min duration were performed, and were comprised of 12 individual on-source and off-source sub-scans of 30 s duration. Observations were interspersed with pointing calibrations taken every 1–3 h on Mars or a bright nearby quasar. Telescope refocusing was carried out approximately every 6 h and following sunset and sunrise. We used the standard reduction software, MIRA, to calibrate each science scan using the calibration scan taken closest in time. Integrations were repeated until a signal was detected, or a sufficient upper limit on a line detection was reached. Multiple integrations were combined in the software package, CLASS, using sigma weighting following first-order baseline subtraction. In general, baselines were calculated using a linear fit in line-free regions typically between [−500, −200] and [200, 500] km s^{-1}, although in a few cases we determined that higher order polynomials were required following visual inspection of the spectra. A small

Table 3. Object name, line intensity, line width, velocity offset from systemic (from the optical spectra), gas masses derived from the CO(1–0) line. These are the values measured from the WILMA spectra and do not include a small aperture correction. The final column lists the CO(1–0) aperture correction based on the *g*-band isophotal radius (see text for details) which can be applied to correct the gas mass to total.

Name	I_{1-0}^a (Jy km s^{-1})	$\Delta V_{(1-0)}$ (km s^{-1})	$\delta v_{sys(1-0)}$ (km s^{-1})	I_{2-1}^b (Jy km s^{-1})	$\Delta V_{(2-1)}$ (km s^{-1})	$\delta v_{sys(2-1)}$ (km s^{-1})	M_{gas} (10^9 M$_\odot$)	f
PSB1	< 1.4	–	–	13.2 ± 2.0	87.4 ± 11.8	-5.1 ± 11.8	< 0.3	1.04 ± 0.28
PSB2	13.8 ± 1.0	146.9 ± 8.9	-13.8 ± 8.9	19.0 ± 3.1	125.0 ± 16.4	83.1 ± 16.3	3.6 ± 0.3	1.12 ± 0.50
PSB3	1.4 ± 0.4	127.4 ± 0.0	0.0 ± 0.0	7.8 ± 2.0	127.4 ± 0.0	0.0 ± 0.0	0.3 ± 0.1	1.08 ± 0.39
PSB4	12.6 ± 1.4	88.9 ± 9.1	22.3 ± 9.1	35.2 ± 2.6	91.5 ± 5.9	31.5 ± 5.9	2.1 ± 0.2	1.12 ± 0.49
PSB5	11.5 ± 0.6	98.6 ± 4.8	3.1 ± 4.8	27.1 ± 2.9	102.1 ± 9.7	52.1 ± 9.7	2.6 ± 0.1	1.03 ± 0.22
PSB6	11.3 ± 1.3	107.5 ± 10.8	14.3 ± 10.8	27.7 ± 3.6	81.1 ± 9.5	18.3 ± 9.5	4.1 ± 0.5	1.05 ± 0.31
PSB7	6.8 ± 1.1	122.1 ± 16.4	-0.4 ± 16.4	7.6 ± 1.7	66.3 ± 13.0	1.2 ± 13.0	3.0 ± 0.5	1.02 ± 0.19
PSB8	1.8 ± 0.4	65.0 ± 10.5	-164.7 ± 10.5	< 5.3	–	–	0.8 ± 0.2	1.02 ± 0.18
PSB9	6.6 ± 0.7	129.5 ± 12.2	36.1 ± 12.2	< 7.3	–	–	3.1 ± 0.3	1.04 ± 0.28
PSB10	8.0 ± 0.9	132.1 ± 12.9	-1.7 ± 12.9	12.9 ± 1.6	64.6 ± 7.2	77.4 ± 7.2	1.9 ± 0.2	1.08 ± 0.39
PSB11	1.4 ± 0.3	< 42.5	-71.7 ± 7.9	6.3 ± 1.4	127.4 ± 0.0	0.0 ± 0.0	0.7 ± 0.1	1.07 ± 0.36

number of scans on PSB1 with significantly higher noise levels were discarded, possibly caused by the worse conditions in which they were taken.

The averaged spectra were smoothed and the channels binned to a velocity resolution of 21 km s^{-1}. Line intensities were measured by summing over the line profile, with a velocity width defined by the full width at half-maximum of a Gaussian fit to the line profile (using least-squares minimization with width, amplitude and centroid free to vary). We estimate the line intensity using a sum under the line profile. Following Young et al. (2011) and Saintonge et al. (2011a) in the case of a non-detection/weak line (i.e. $<4\sigma$), we calculated upper limits by summing over a velocity width of 300 km s^{-1} centred on the systemic velocity of the galaxy measured from the SDSS spectrum.

We determined the statistical uncertainty on each line intensity (σ_I^2) following Sage, Welch & Young (2007) and Young et al. (2011) as

$$\sigma_I^2 = (\Delta v)^2 \sigma^2 N_l \left(1 + \frac{N_l}{N_b} \right), \qquad (1)$$

for a line of width Δv with N_l line channels and N_b baseline channels. The rms noise level σ is equal to the standard deviation of the flux measured in line-free regions. Where a line was not detected at $>4\sigma$, we define an upper limit as four times the statistical uncertainty of the integrated line intensity. 10/11 PSBs were detected with $>4\sigma$ significance in the CO(1–0) transition and 9/11 PSBs in the CO(2–1) transition. Table 3 presents the CO line measurements and Fig. B1 shows the observed spectra.

Conversion from antenna temperature to main beam brightness temperature was achieved using the ratio of the beam and forward efficiencies $B_{eff}/F_{eff} = 0.83$ at 2.6 mm and 0.64 at 1.3 mm.[3] We then converted from main beam temperature to flux assuming a factor of 4.73 Jy K^{-1}. Gas masses were estimated from the CO(1–0) line flux using a Galactic CO to H$_2$ conversion factor $\alpha_{CO} = 3.2$ M$_\odot$ (K km s^{-1} pc^2)$^{-1}$, with an additional factor of 1.36 for helium.

Given the optical extent of the galaxies, it is possible that the CO beam ($\sim$22 arcsec at 115 GHz and $\sim$11 arcsec at 230 GHz) does not encompass all of the emission. We compute aperture corrections (f) following Lisenfeld et al. (2011) and Stark et al. (2013) assuming

that the CO distribution follows an exponential disc with scalelength given by the *g*-band isophotal radius. The aperture corrections are typically small, with a median correction of 10 per cent at 115 GHz and 20 per cent at 230 GHz. Where we aperture correct CO fluxes and gas masses, we add in quadrature to the errors 5 per cent of the *g*-band size, to account for the uncertainty of aperture correction. Whether we choose to apply aperture corrections or not does not change our conclusions. This is because the optical size of the PSBs is often comparable to or slightly smaller than the half-power beam width at 115 GHz, meaning that the aperture correction is small. In the following results, we use aperture corrected line fluxes and gas masses unless explicitly stated.

3.3 *Herschel* data

The *Herschel* (Pilbratt et al. 2010) data were obtained from the OT1_vwild_1 open time programme. All PSBs were observed with the PACS (Poglitsch et al. 2010) and SPIRE (Griffin et al. 2010) instruments in scan map mode in six bands at 70, 100, 160, 250, 350 and 500 µm with a medium scan speed of 20 arcsec s^{-1}. We use the SCANAMORPHOS map-maker (Roussel 2013), implemented in version 12 of HIPE (Ott 2010), to mitigate the low-frequency 1/*f* noise in the PACS data, whilst preserving extended source emission. The same version of HIPE was used to create the SPIRE maps, with the naïve map-maker being used in this case.

PACS and SPIRE fluxes were determined by summing the flux within a circular aperture centred on the peak flux of the source. We used apertures with radii of 12, 12, 22, 22, 30 and 40 arcsec corresponding to 12, 12, 11, 3.7, 3.0 and 2.9 pixels at 70, 100, 160, 250, 350 and 500 µm, respectively. To estimate the background, we used annuli with inner and outer radii of 35 and 45 arcsec for flux densities at 70–160 µm and 60 and 90 arcsec for flux densities at 250–500 µm. We applied the aperture corrections as recommended in the PACS[4] and SPIRE[5] observers manuals for the FM7 calibration.[6] For SPIRE sources, we assume beam areas of 436, 772 and 1590 arcsec^2 at 250, 350 and 500 µm, which include a correction for point sources with a flux density assumed to be dependent on the spectral index as $S_\nu \sim \nu^{3.5}$. One object, PSB8, was found to lie in a crowded field,

---

[3] http://www.iram.es/IRAMES/mainWiki/Iram30mEfficiencies

[4] http://herschel.esac.esa.int/Docs/PACS/html/pacs_om.html
[5] http://herschel.esac.esa.int/Docs/SPIRE/html/spire_handbook.html
[6] 1.247, 1.289, 1.224, 1.261, 1.226, 1.202.

with the standard aperture at 160 μm overlapping a neighbouring source. For this object, we reduced the aperture radius by a factor of 2 for the 160 μm observations, increasing the aperture correction accordingly. For observations at ≥250 μm, we set the fluxes to upper limits at the measured flux values. The observing strategy required to obtain both 70 and 100 μm maps means that two independent maps were obtained at 160 μm. We treated the two 160 μm maps independently, deriving flux densities which were combined using sigma weighting. In all cases, the independent 160 μm fluxes agree to within the 1σ errors. We also apply the standard colour corrections for point sources from the SPIRE observers manual of 0.8930, 0.8978, 0.8757 assuming that the flux density can be described as $S_\nu \sim \nu^{3.5}$ in the Rayleigh–Jeans (R–J) regime.

We determined the uncertainties on the PACS flux densities following Balog et al. (2014), by measuring the signal rms in the background annulus used for sky subtraction in each band. We correct for the correlated noise between pixels which results from regridding the data from the detector pixel size on to pixels projected on the sky. The noise increases by a factor of 3.4, 3.2 and 8.0. We use this method of error estimation as it results in a higher (more conservative) estimate of the noise than those using the standard deviation of the flux density measured in six sky apertures.

For the SPIRE fluxes, following Ciesla et al. (2012) the total error ($\sigma_{\rm tot}$) encompasses the instrumental error ($\sigma_{\rm inst}$), the sky background error ($\sigma_{\rm sky}$) and the confusion error ($\sigma_{\rm conf}$), and is calculated as

$$\sigma_{\rm tot} = \sqrt{\sigma_{\rm inst}^2 + \sigma_{\rm sky}^2 + \sigma_{\rm conf}^2}. \quad (2)$$

For SPIRE data, $\sigma_{\rm inst}$ was calculated by summing in quadrature the values on the error map within the same aperture as the source. For each SPIRE band, we estimated the sky background noise level ($N_{\rm pix}\sigma_{\rm skymean}$) by measuring the standard deviation of the mean sky value in each aperture around the source, using 16 apertures at 250 and 350 μm, and eight apertures at 500 μm with the same size as the source aperture, where $N_{\rm pix}$ is the number of pixels in the aperture. For the SPIRE maps, we adopt the confusion noise estimates (err$_{\rm conf}$) from Nguyen et al. (2010) of 5.8, 6.3 and 6.8 mJy beam^{-1} at 250, 350 and 500 μm, respectively. The confusion error is

$$\sigma_{\rm conf} = {\rm err}_{\rm conf} \times \sqrt{\frac{N_{\rm pix} \times {\rm pixsize}^2}{\rm beamarea}}, \quad (3)$$

following Ciesla et al. (2012). The confusion noise at the depth of the PACs maps is negligible. We convolve the uncertainties in quadrature with a flux calibration error of 5 and 5.5 per cent of the PACS[7] and SPIRE fluxes, respectively, as recommended in the PACS and SPIRE manuals, (Bendo et al. 2013). Following Smith et al. (2013), we use all positive flux measurements in each band regardless of the signal to noise in order to include as much information as possible in the SED. Where a negative flux is measured, we include the flux as an upper limit consistent with a flux density of zero.

3.4 Ancillary data

For each source, we compile far-ultraviolet (FUV) and near-ultraviolet (NUV) data from the *GALEX* DR7 catalogue server. All sources are matched to the nearest source within a 3 arcsec radius. We reject fluxes which have artefact flags and where the source is too close to the detector edge for reliable flux measurements

(field-of-view radius >0°.55). Where multiple observations exist, we select the deepest observation. We correct the UV fluxes for galactic extinction using the values of $E(B-V)$ from Schlegel, Finkbeiner & Davis (1998) and the factor $A_{\rm FUV} = 7.9E(B-V)$ and $A_{\rm NUV} = 8.0E(B-V)$, derived using the Cardelli, Clayton & Mathis (1989) Galactic extinction law for a total-to-selective extinction ratio of $R_V = 3.1$. Non-detections ($<5\sigma$) are included as upper limits in the SED fitting.

We compile near-infrared *J*, *H* and *K* elliptical isophotal magnitudes from the Two Micron All Sky Survey (Skrutskie et al. 2006) Extended Source Catalog (Jarrett et al. 2000). We also compile *Wide-field Infrared Space Explorer* (*WISE*; Wright et al. 2010) $3-22$ μm fluxes from the all-sky data release. We use the profile mags (*w4mpro*) for point sources (defined with ext_flg = 0), and the aperture magnitudes (*w4gmag*) for extended sources. Following Jarrett et al. (2012), we add small zero-point corrections of 0.03, 0.04, 0.03 and −0.03 to the *WISE* *W*1, *W*2, *W*3 and *W*4 magnitudes, respectively. We convert the *WISE* magnitudes to fluxes including a colour correction dependent on the spectral slope.[8] We apply a further colour correction to the *W*4 band as our sources have rising spectral slopes in this band, following the updated calibration in Brown et al. (2014). Where fluxes are not detected in the *WISE* bands we utilize upper limits in the SED fitting at the 2σ level.

We compiled fluxes from the *IRAS* Faint Source Catalogue (Moshir 1989) at 25 and 60 μm which have a quality flag >2. Where fluxes were of low quality or undetected, we used 5σ upper limits of 0.2 Jy in the SED fitting.

In the UV, optical, near- and mid-infrared fluxes, we convolve the catalogue error in quadrature with a calibration error of 20, 10, 15 and 10 per cent of the flux, respectively, to allow for differences in the methods used to measure total photometry and errors in the spectral synthesis models used to fit the underlying stellar populations. To account for larger calibration uncertainty in the *WISE* *W*4 band, we convolve the catalogue error in quadrature with 20 per cent of the measured, colour-corrected flux.

3.5 SED fitting

The wealth of multiwavelength data for our sample of PSBs allows us to derive global physical properties by fitting models to their broad-band photometric SEDs. We use the physically motivated method of da Cunha, Charlot & Elbaz (2008, hereafter DCE08[9]) to recover the physical properties of the PSBs.

DCE08 employ an energy balance prescription, whereby the UV–optical radiation emitted by stellar populations is absorbed by dust, and this absorbed energy is matched to that re-radiated in the FIR. The optical library of 50 000 spectra is produced using the latest version of the population synthesis code of Bruzual & Charlot (2003), Charlot & Bruzual (in preparation), and assumes exponentially declining SFHs with additional superimposed random bursts (known as stochastic SFHs). The model spectra cover a wide range of age, metallicity, SFH and dust attenuation and a Chabrier (2003) is assumed. The infrared libraries contain 50 000 SEDs comprised of four different temperature dust components. In stellar birth clouds, these components are polycyclic aromatic hydrocarbons, hot dust (stochastically heated small grains with a temperature 130–250 K) and warm dust in thermal equilibrium (30–60 K). In the diffuse ISM, the relative fractions of these three dust components are fixed, but

---

[7] Note that due to the uncertainty in the appropriate colour correction, the PACS flux could be uncertain by up to 20 per cent.

[8] http://wise2.ipac.caltech.edu/docs/release/allsky/expsup/sec4_4h.html

[9] The DCE08 models are publicly available as a user-friendly model package MAGPHYS at www.iap.fr/magphys/

Table 4. Physical parameters derived from fitting the UV to FIR SEDs of each galaxy. The columns are (from left to right): Name, $M_*/M_\odot$, $\log_{10}$(stellar mass); $M_d/M_\odot$, $\log_{10}$(dust mass); M_d/M_*, $\log_{10}$(dust-to-stellar mass ratio); T_C^{ISM}/K, temperature of the cold diffuse ISM dust component; $L_d/L_\odot$, $\log_{10}$(dust luminosity); SFR/$M_\odot$ yr^{-1}, the $\log_{10}$(SFR) averaged over the last 10^8 yr and SSFR/yr^{-1}, the $\log_{10}$(SSFR) averaged over the last 10^8 yr. Uncertainties are indicated by the median 84th–16th percentile range from each individual parameter PDF. Note that T_C^{ISM} should be treated with caution as the median likelihood values are close to the bounds on the temperature prior.

Name	M_* $\log_{10}(M_\odot)$	M_d $\log_{10}(M_\odot)$	M_d/M_* $\log_{10}(M_d/M_*)$	T_C^{ISM} (K)	L_d $\log_{10}(L_\odot)$	SFR $\log_{10}(M_\odot yr^{-1})$	SSFR $\log_{10}(yr^{-1})$
PSB1	$9.33^{+0.15}_{-0.03}$	$7.32^{+0.09}_{-0.03}$	$-2.01^{+0.06}_{-0.16}$	$23.8^{+1.2}_{-0.7}$	$11.00^{+0.02}_{-0.01}$	$1.04^{+0.04}_{-0.03}$	$-8.27^{+0.01}_{-0.15}$
PSB2	$10.48^{+0.06}_{-0.01}$	$7.61^{+0.01}_{-0.01}$	$-2.88^{+0.01}_{-0.05}$	$24.6^{+0.1}_{-0.1}$	$11.36^{+0.01}_{-0.01}$	$1.21^{+0.15}_{-0.01}$	$-9.27^{+0.10}_{-0.01}$
PSB3	$9.50^{+0.05}_{-0.04}$	$6.93^{+0.12}_{-0.06}$	$-2.55^{+0.13}_{-0.10}$	$23.8^{+0.7}_{-2.2}$	$10.62^{+0.04}_{-0.09}$	$0.74^{+0.05}_{-0.04}$	$-8.77^{+0.10}_{-0.05}$
PSB4	$9.81^{+0.01}_{-0.07}$	$7.45^{+0.03}_{-0.03}$	$-2.34^{+0.07}_{-0.03}$	$24.3^{+0.5}_{-0.4}$	$10.84^{+0.01}_{-0.02}$	$0.74^{+0.01}_{-0.02}$	$-9.07^{+0.10}_{-0.01}$
PSB5	$9.46^{+0.08}_{-0.06}$	$7.23^{+0.01}_{-0.01}$	$-2.24^{+0.08}_{-0.09}$	$24.1^{+0.6}_{-0.1}$	$10.86^{+0.01}_{-0.03}$	$0.80^{+0.03}_{-0.04}$	$-8.68^{+0.10}_{-0.20}$
PSB6	$10.47^{+0.02}_{-0.15}$	$7.50^{+0.08}_{-0.14}$	$-2.95^{+0.11}_{-0.15}$	$21.4^{+1.5}_{-0.3}$	$10.58^{+0.04}_{-0.02}$	$0.40^{+0.07}_{-0.03}$	$-10.07^{+0.24}_{-0.01}$
PSB7	$10.08^{+0.09}_{-0.02}$	$6.91^{+0.06}_{-0.05}$	$-3.18^{+0.08}_{-0.09}$	$24.6^{+0.3}_{-0.8}$	$10.24^{+0.05}_{-0.02}$	$-0.13^{+0.04}_{-0.02}$	$-10.22^{+0.05}_{-0.05}$
PSB8	$9.89^{+0.15}_{-0.11}$	$6.41^{+0.27}_{-0.18}$	$-3.47^{+0.30}_{-0.23}$	$22.9^{+1.5}_{-2.5}$	$9.57^{+0.05}_{-0.08}$	$-0.94^{+0.18}_{-0.23}$	$-10.87^{+0.25}_{-0.25}$
PSB9	$10.11^{+0.03}_{-0.10}$	$7.19^{+0.08}_{-0.10}$	$-2.92^{+0.14}_{-0.12}$	$23.1^{+1.1}_{-1.0}$	$10.23^{+0.03}_{-0.02}$	$-0.16^{+0.11}_{-0.01}$	$-10.22^{+0.05}_{-0.05}$
PSB10	$10.04^{+0.05}_{-0.23}$	$7.24^{+0.02}_{-0.02}$	$-2.79^{+0.22}_{-0.06}$	$24.6^{+0.2}_{-0.2}$	$10.57^{+0.01}_{-0.04}$	$0.23^{+0.06}_{-0.04}$	$-9.82^{+0.30}_{-0.05}$
PSB11	$10.49^{+0.03}_{-0.06}$	$7.03^{+0.23}_{-0.27}$	$-3.46^{+0.23}_{-0.28}$	$19.5^{+2.2}_{-1.8}$	$9.70^{+0.03}_{-0.06}$	$-0.82^{+0.03}_{-0.07}$	$-11.32^{+0.10}_{-0.05}$

an additional cold dust component with an adjustable temperature between 15 and 25 K is added. The dust mass absorption coefficient $\kappa_\lambda \propto \lambda^{-\beta}$ has a normalization of $\kappa_{850} = 0.077 \, m^2 \, kg^{-1}$ (Dunne et al. 2000). A dust emissivity index of $\beta = 1.5$ is assumed for warm dust, and $\beta = 2.0$ for cold dust.

Statistical constraints on the various parameters of the model are derived using the Bayesian approach described in DCE08, which ensures that possible degeneracies between model parameters are included in the final probability density function (PDF) of each parameter. The effects of individual wavebands on the derived parameters are explored in DCE08 and Smith et al. (2012). The MAGPHYS code used in this paper has been modified from the public version to take into account flux density upper limits in the χ^2 calculation to give additional constraints on physical parameters, as described in Smith et al. (2012) and Rowlands et al. (2014a). For more details of the method, we refer the reader to DCE08.

The best-fitting SEDs are shown in Fig. C1, and the fitted values and errors on the main parameters of interest are provided in Table 4. In Fig. 3, we compare the total SFR derived from the SED fitting (averaged over the last 10^8 yr) to the SFR in the central 3 arcsec fibre derived from the dust-corrected Hα emission. There is a very good agreement between the two measurements over the wide range of SFR probed; however; there is an offset with the total SFR higher than the fibre SFR by around a factor of 2 on average. This may be due to: (1) the fibre only covering the inner 0.9–1.4 kpc in radius (30–100 per cent of the r-band half-light radius, and 10-30 per cent of the r-band Petrosian R_{90} radius); (2) the Hα-derived SFR is not exactly equivalent to a SFR derived from SED fitting, and in particular relates to an average over a shorter time interval; (3) the extinction corrected Hα may underestimate the true SFR in the mostly heavily extincted sites of star formation. It is therefore difficult to draw any firm conclusions about the distribution of star formation in the galaxies from these observations. In the following results, we consider the total SFR, unless stated otherwise.

4 RESULTS

In WHC10, we used the full sample of local ($z < 0.07$) bulge-dominated SDSS galaxies to study the black hole accretion activity
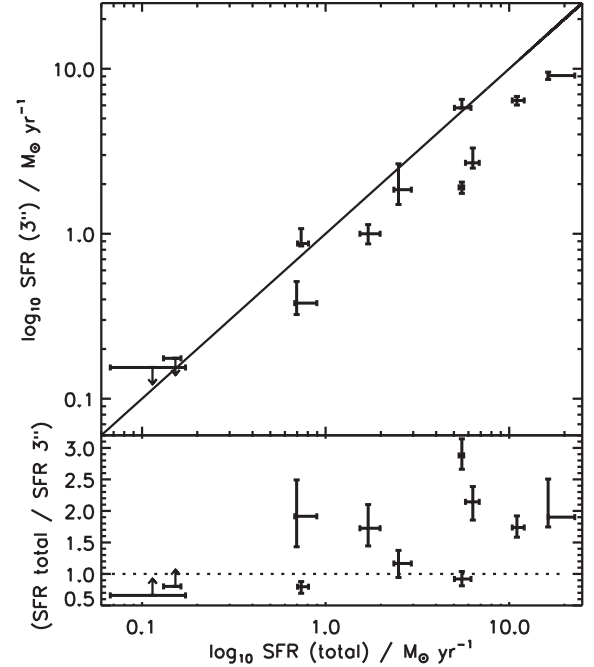

Figure 3. Comparison of the total SFR from multiwavelength SED fitting and the 3 arcsec SFR (0.9–1.4 kpc in radius), from the dust-corrected Hα luminosity. The solid line is the one-to-one relation. The lower plot shows the ratio of total SFR to 3 arcsec SFR as a function total SFR. In the lower panel, we account for the propagation of asymmetric error values via a Monte Carlo analysis. The total SFR is on average slightly higher than the fibre SFR by around a factor of 2.

as a function of starburst age ('Timing the starburst-AGN connection'). Here, we wish to address very specifically the question of *how and why* star formation declines following a starburst, which is currently very poorly constrained observationally.
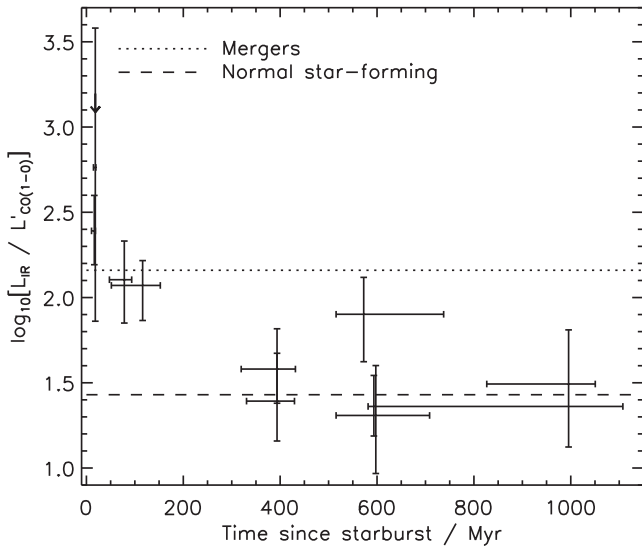
Figure 4. The ratio of FIR luminosity (L_{FIR}) to CO(1–0) luminosity (a proxy for SFE), as a function of starburst age. A clear trend of decreasing $L_{FIR}/L'_{CO(1–0)}$ with starburst age is observed. The dotted line shows the average value of $L_{FIR}/L'_{CO(1–0)}$ for IR luminous mergers and the dashed line shows the average value for normal galaxies from Genzel et al. (2010).

4.1 Star formation efficiency

The star formation efficiency (SFE) quantifies how quickly gas is consumed by star formation. For consistency with previous work, we begin this section by plotting in Fig. 4 the ratio of FIR luminosity (L_{FIR}; the integrated emission between 3 and 1000 μm) to the CO line luminosity ($L'_{CO(1–0)}$; Solomon & Vanden Bout 2005), as a function of starburst age. Under the assumption that L_{FIR} corresponds to total SFR[10] and $L'_{CO(1–0)}$ traces the gas mass, the ratio of these quantities is a proxy for the SFE.

We find that the young PSBs have $L_{FIR}/L'_{CO(1–0)}$ values around a factor of 5 higher than the older PSBs. This is similar to the difference found between interacting and isolated galaxies (a factor of 4–6; Young et al. 1986; Lisenfeld et al. 2011). The $L_{FIR}/L'_{CO(1–0)}$ of the young PSBs is consistent with IR luminous mergers/starbursts ($L > 10^{11}$ L$_\odot$) from Genzel et al. (2010), even though the PSBs have a lower FIR luminosity (likely as a result of their lower mean stellar mass compared to typical Luminous Infared Galaxies (LIRGs) ($M_* > 10^{10}$ M$_\odot$). Over a time-scale of ∼300 Myr, the $L_{FIR}/L'_{CO(1–0)}$ falls, and is consistent with that of normal star-forming galaxies for the older PSBs (Genzel et al. 2010). We do not find PSBs with $L_{FIR}/L'_{CO(1–0)}$ similar to those of gas-rich ETGs, which have a $L_{FIR}/L'_{CO(1–0)}$ a factor of 2.5 lower than normal spiral galaxies (Davis et al. 2014). It is clear that by 0.5–1 Gyr following the starburst, the star formation is not completely quenched and the star formation remains relatively efficient. It is interesting to note that the time around which the decrease in $L_{FIR}/L'_{CO(1–0)}$ occurs is coincident with a significant increase in the black hole accretion rate in PSBs (WHC10); however, this correlation does not imply any causation.

The molecular gas depletion time is inversely proportional to the SFE. In Fig. 5, we plot the molecular gas depletion time in years ($\tau_{dep} = M_{gas}/SFR$) as a function of starburst age. Here, we replace
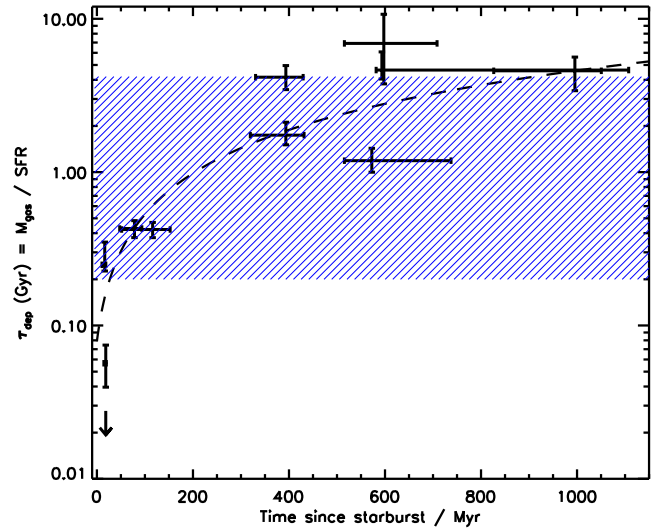

Figure 5. The molecular gas depletion time ($\tau_{dep} = M_{gas}/SFR$ from MAGPHYS) as a function of starburst age for the PSBs. The dotted line shows the relation for a linear increase in depletion time with starburst age. The blue-hatched area indicates the typical molecular gas depletion time-scales for 30 nearby disc galaxies from Leroy et al. (2013).

L_{FIR} with the SFR measured from the full multiwavelength SED fit, to be consistent with most recent literature. We observe a clear trend of increasing molecular gas depletion time with starburst age, which is best fit by the linear relation

$$\tau_{dep}/10^9 = 0.0045t_{SB} + 0.078, \tag{4}$$

where τ_{dep} is in Gyr, and t_{SB} is in Myr. We note that this trend is analogous to that seen between $L_{FIR}/L'_{CO(1–0)}$ and starburst age in Fig. 4, and therefore the observed trend is independent of the choice of α_{CO}. We measure depletion times of ∼1–8 Gyr for the oldest PSBs, in agreement with those of normal spiral galaxies of a similar stellar mass (Bigiel et al. 2008; Leroy et al. 2008, 2013; Saintonge et al. 2011b; Huang & Kauffmann 2014). This suggests that the depletion times of PSBs are returning to normal after a burst of star formation, although we are unable to tell whether they will continue to decline in the future with the present sample. The younger PSBs have shorter depletion times of 50–500 Myr, consistent with those of IR luminous mergers ($\tau_{dep} \sim 200$ Myr; Genzel et al. 2010).

Many studies have now demonstrated that IR luminous mergers/starburst galaxies exhibit an excess SFR relative to their molecular gas content (and hence have a shorter depletion time), when compared to normal star-forming galaxies (Sanders et al. 1991; Sanders & Mirabel 1996; Gao & Solomon 2004; Daddi et al. 2010; Genzel et al. 2010). Two alternative scenarios exist to explain this result. (1) During the interaction/merger gas may be driven into the centre by tidal torques, leading to higher gas surface densities and more efficient star formation (Braine & Combes 1993; Downes & Solomon 1998; Tacconi et al. 2008). (2) The molecular gas reservoir has been depleted and the starburst quenched, but the FIR emission is still visible (Leroy et al. 2006). As our measurement of depletion time does not depend directly on the L_{FIR}, and we have shown that the SFR measured from the multiwavelength SED tracks that measured by dust-corrected Hα luminosity which provides a close to instantaneous measure of SFR, we strongly favour the first option. In principle, the combination of stellar population age measured from the stellar continuum, Hα luminosity and L_{FIR}, provides a powerful constraint on the decay rate of L_{FIR} following a starburst. The fact

---

[10] This may not be true for galaxies no longer undergoing a starburst, but this would only reinforce the trend in Fig. 4 since the infrared luminosity would overpredict the SFR (see Rowlands et al. 2014a).
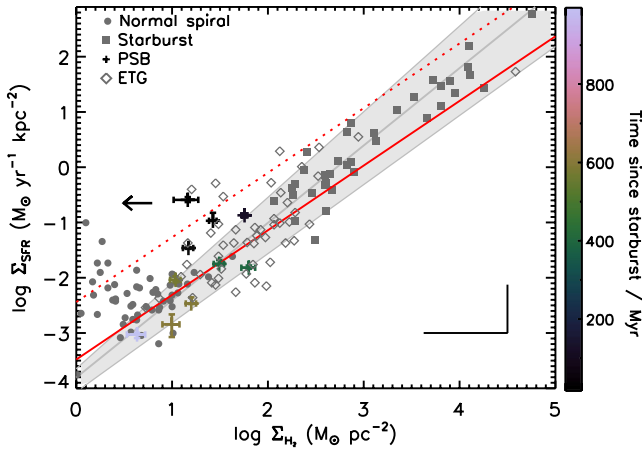
Figure 6. The SFR surface density ($\Sigma_{\rm SFR}$) as a function of molecular gas mass surface density ($\Sigma_{\rm H_2}$) for the PSBs (crosses), with points colour coded by starburst age. Grey circles show normal star-forming galaxies, and grey squares show circumnuclear starbursts from K98 (corrected down by a factor of 1.6 to a Chabrier IMF). ETGs with molecular gas (and H I gas, although this is negligible) are shown as unfilled diamonds (Davis et al. 2014). All values of $\Sigma_{\rm H_2}$ assume a Galactic CO conversion factor, and literature values have been corrected to a common value of $\alpha_{\rm CO} = 4.35\,{\rm M_\odot}\,({\rm K\,km\,s^{-1}\,pc^2})^{-1}$. The grey line shows the K–S relation (with the scaling factor corrected downwards by a factor of 1.6 to a Chabrier IMF), with the 1σ scatter as the grey filled area. The red lines indicate the relation for star-forming galaxies (solid) and mergers (dotted) from Genzel et al. (2010). The black horizontal and vertical bar indicates the median possible systematic in the SFR and gas surface densities when using the u-band Petrosian R_{50} instead of the R_{90} radius.

that we find no significant offset in time-scales between the decay in SFE implied by Figs 4 and 5 rules out the possibility that the FIR emission remains visible for an extended period following the starburst. However, larger numbers of galaxies would be required to determine precisely the impact of using $L_{\rm FIR}$ to infer star formation efficiencies and depletion times.

4.2 Kennicutt–Schmidt relation

Gas mass surface density ($\Sigma_{\rm H_2}$) and SFR surface density ($\Sigma_{\rm SFR}$) in galaxies are linked by the Kennicutt–Schmidt (K–S) relation (K98). In Fig. 6, we plot the molecular $\Sigma_{\rm H_2}$ and $\Sigma_{\rm SFR}$ for the PSBs and compare them to normal star-forming galaxies and circumnuclear starbursts from K98, and ETGs with molecular gas from Davis et al. (2014). For the PSBs, we do not have resolved CO or SFR observations so we assume that the CO emitting region is the same as where young stars are located, and use the u-band Petrosian R_{90} radius as the area over which we calculate $\Sigma_{\rm H_2}$ and $\Sigma_{\rm SFR}$. This approximation leads to a substantial uncertainty in both parameters: a factor of 2 decrease in the radius for star formation and gas emission (i.e going from Petrosian R_{90} to R_{50} radius) shifts the PSBs $\sim$1 dex to the upper right of the plot. All $\Sigma_{\rm H_2}$ estimates assume a Galactic CO-to-H$_2$ conversion factor, although Genzel et al. (2010) suggest a lower value of $\alpha_{\rm CO}$ may be appropriate for IR luminous mergers. Adopting a lower value of $\alpha_{\rm CO}$ would decrease the gas surface density of the PSBs.

Under the assumptions of size and $\alpha_{\rm CO}$ made above, we find that the PSBs sit in an intermediate region between normal star-forming spirals and circumnuclear starbursts. There is a clear trend of starburst age relative to position on the K–S relation. The youngest PSBs with an age <100 Myr have the highest SFR and gas mass surface

densities, and lie in a region coincident with ETGs with molecular gas (Davis et al. 2014), and have slightly lower gas mass and SFR surface densities than local circumnuclear starbursts (K98). Note that only 22 per cent of all ETGs in the local Universe (<42 Mpc) harbour a detectable mass of molecular gas, so PSBs have a much higher gas mass surface density than the vast majority of ETGs (those not plotted here).

The higher gas surface densities of the young PSBs (which are the most morphologically disturbed) relative to normal galaxies is consistent with Braine & Combes (1993) and Downes & Solomon (1998), who found higher gas surface densities in interacting systems. The increased gas surface density could be a result of the funnelling of gas into the central regions during interactions/mergers (e.g. Mihos & Hernquist 1994, 1996; Barnes & Hernquist 1996). Observations of dense gas tracers in young PSBs would help confirm this hypothesis (Gao & Solomon 2004). Beyond the $\sim$600 Myr timespan of our observations, it is unclear whether the PSBs will continue to evolve back to the region occupied by the spirals, or exhaust their gas supplies to become gas-poor ETGs. More observations of the gas content of PSBs older than 600 Myr are needed in order to examine the late-time evolution of this population.

Note that we do not consider the total (neutral and atomic) gas surface density in this work, as only three PSBs have detections of H I gas [PSB4, PSB5 and PSB11 from Davoust & Contini (2004) and the ALFALFA survey (Haynes et al. 2011)], an additional three PSBs have upper limits from the Northern HIPASS Catalogue (Wong et al. 2006, 2009) which do not put strong constraints on the H I gas mass. In normal galaxies, there is a large variation in H$_2$/H I mass (Saintonge et al. 2011b), therefore we cannot reliably predict H I from H$_2$ in the PSBs. The detection of substantial atomic gas reservoirs in some PSBs indicates that either the H I reservoir has not been depleted (Zwaan et al. 2013), or re-accretion of gas can occur after the star formation has been quenched (Saintonge et al. 2011a; Stark et al. 2013; Yates & Kauffmann 2014), which may be particularly efficient in low-mass systems (Saintonge et al. 2011b). Alternatively, H I gas exists in the outer disc and is not affected by the starburst and subsequent quenching event in the central region (Saintonge et al. 2011b; Pracy et al. 2014).

4.3 Cold ISM content

In this section, we discuss the physical properties of the cold ISM of PSBs. From the MAGPHYS SED fitting, we derive a range of dust masses from $0.3 - 4.0 \times 10^7\,{\rm M_\odot}$, with a median dust mass of $1.7 \times 10^7\,{\rm M_\odot}$. This is similar to that of low-redshift spiral galaxies with a similar stellar mass to the PSBs in the *Herschel*-ATLAS (Rowlands et al. 2012). The median molecular gas mass derived from the 12CO(1–0) integrated line fluxes is $2.7 \times 10^9\,{\rm M_\odot}$ with a range from $(< 0.3$–4.3$) \times 10^9\,{\rm M_\odot}$, assuming a Galactic CO to H$_2$ conversion factor. The molecular gas masses of the PSBs are similar to those of the most gas-rich ETGs (Young et al. 2011) and spiral galaxies (Lisenfeld et al. 2011) in the local Universe (see also French et al. 2015).

4.3.1 Gas-to-stellar mass

In Fig. 7(a), we show the gas-to-stellar mass ratio ($M_{\rm gas}/M_*$) of the PSBs as a function of starburst age, which ranges from 0.02 to 0.92 with a median of 0.18. The gas-to-stellar mass ratios of the majority of the PSBs are consistent with the range found for
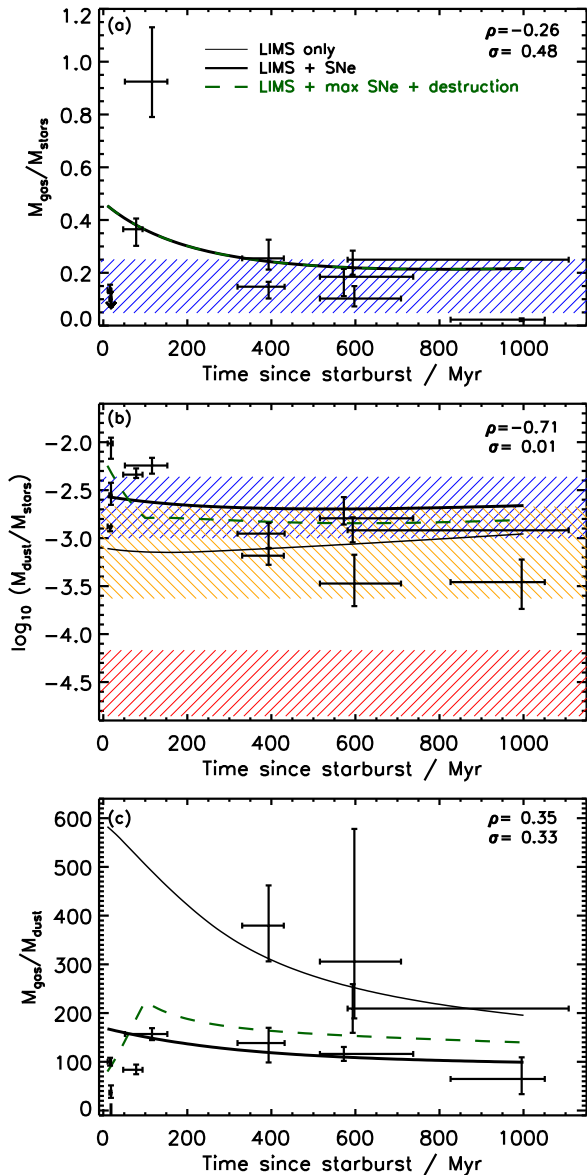
Figure 7. (a) Molecular gas-to-stellar mass ratio as a function of starburst age. We observe a wide range of gas-to-stellar mass ratios in both young and old PSBs. The blue-hatched region is the range of observed gas-to-stellar mass ratios for normal nearby galaxies ($\sim$0.1 for CO detected galaxies of a similar stellar mass to the PSBs; $M_* \sim 10^{10}\,\mathrm{M}_\odot$; Saintonge et al. 2011a; Boselli et al. 2014). (b) Dust-to-stellar mass ratio versus starburst age. The blue-hatched region is the standard deviation either side of the mean M_d/M_* for $z < 0.1$ spiral galaxies detected in the *Herschel*-ATLAS (Rowlands et al. 2012). The orange-hatched region is the standard deviation either side of the mean M_d/M_* for $z < 0.06$ dusty ETGs from Agius et al. (2013), using updated FIR photometry. The red-hatched region is the range of M_d/M_* for non-dusty ETGs (representative of red-sequence galaxies) for a range of dust temperatures (Rowlands et al. 2012). (c) Gas-to-dust mass ratio as a function of starburst age. Values in the right of each plot indicate the non-parametric Spearman rank coefficient (ρ) and the two-sided significance of the deviation of the correlation from zero, or the null hypothesis (σ, a low value indicates a significant correlation). On each plot, we show closed-box chemical evolution models with dust produced by LIMS only with no destruction (thin black line), LIMS+SNe with no destruction (thick black line) and dust from LIMS+SNe (green dashed line; assuming all metals are converted into dust) with strong destruction from 0–0.1 Gyr and weak destruction from 0.1–1.0 Gyr. Note that the chemical evolution models are not fits to the data.

normal nearby galaxies ($\sim$0.1 for CO detected galaxies;[11] Boselli et al. 2014) of a similar stellar mass to the PSBs ($M_* \sim 10^{10}\,\mathrm{M}_\odot$; see also Saintonge et al. 2011a). The gas-to-stellar mass ratios of the PSBs are on average a factor of 20 higher than those of red-sequence galaxies ($NUV - r = 6$) which have a typical gas-to-stellar mass ratio of 0.012 (Saintonge et al. 2011a). However, local red-sequence samples will be dominated by objects with higher stellar masses, which have lower gas-to-stellar mass ratios. For a detailed comparison, a mass-matched sample would be essential. The gas-to-stellar mass ratios of the PSBs are also greater than those of ETGs in the *Herschel* Reference Survey ($M_{gas}/M_* \sim 5.3 \times 10^{-3}$; Boselli et al. 2014) and in the ATLAS[3D] sample with detected molecular gas (Cappellari et al. 2013). The ATLAS[3D] ETGs have gas-to-stellar mass ratios[12] ranging from 8.9×10^{-5} to 5.6×10^{-3}, with an average of 7.1×10^{-4}.

Fig. 7(a) also shows that there is no significant correlation of the gas-to-stellar mass ratio with time since the starburst ended (Spearman correlation coefficient $\rho = -0.26$, with the two-sided significance of the deviation of the correlation from zero, or the null hypothesis $\sigma = 0.48$), although there is a large scatter in our sample. This suggests that the majority of gas may have already been consumed in the starburst and we are just observing the residual gas reservoir. Alternatively, the global molecular gas reservoir may not be affected by a nuclear starburst event (Pracy et al. 2014) and only gas in the central region ($\sim$2 kpc for the galaxies here) may be consumed by star formation or affected by feedback processes from star formation or an AGN. High spatial resolution mapping of the molecular gas is needed to determine this.

Over time, one may expect a slow depletion of the gas reservoir due to star formation, with typical time-scales of 0.3 Gyr related to disc dynamical time-scales (Lehnert & Heckman 1996, K98). A much larger sample may be required to observe this expected decline, given the typical errors on gas mass measurements at these redshifts. A rapid decline in gas-to-stellar mass ratio at early times, which would indicate expulsion of gas by SNe and/or fast stellar winds, is not observed. A later rapid decline, which would be the smoking gun for the heating or expulsion of gas from an accreting supermassive black hole, is also not observed. Our results disagree with those of Schawinski et al. (2009), who suggested that in ETGs the molecular gas mass drops 200 Myr after the starburst, interpreting this as evidence that low-luminosity AGN are responsible for the destruction of the gas reservoir. We note that their sample is not directly comparable to ours as their ETGs are classified spectroscopically as blue-sequence (normal star-forming) galaxies and not PSBs, and therefore there is no well-defined age for the stellar population as is the case for PSB galaxies.

The presence of substantial molecular gas reservoirs in the 600-Myr old PSBs suggests that these galaxies are still capable of forming stars and are not entering the red sequence. The oldest PSB (PSB11) has a gas-to-stellar mass ratio of 0.02, still significantly higher than ETGs found in the literature. If low-redshift PSBs ultimately lead to red-sequence galaxies, these results imply a transition time-scale of more than 1 Gyr. We can conclude that the PSBs are not transitioning to the red sequence any more rapidly than the

---

[11] Note that including CO non-detections decreases the average gas-to-stellar mass ratio to $\sim$0.04.

[12] Where the stellar mass is the Jeans anisotropic mass, i.e the total stellar mass from dynamical modelling, and should be comparable to our SED-derived M_* within a factor of 2.

Milky Way (MW) or any other local nearby spiral (Leroy et al. 2013).

4.3.2 Dust-to-stellar mass ratio

The median dust-to-stellar mass ratio (M_d/M_*) of the PSBs is 1.3×10^{-3} with a range of $(0.3–10.0) \times 10^{-3}$, similar to dusty galaxies in the local Universe (Smith et al. 2012). In Fig. 7(b), we compare the dust-to-stellar mass ratios of the PSBs to those of other galaxies, as a function of starburst age. We observe a significant decrease in the dust-to-stellar mass ratio of the PSBs with starburst age (Spearman coefficient $\rho = -0.71, \sigma = 0.01$). The dust-to-stellar mass ratios of the young PSBs are slightly higher than those of spiral galaxies in the H-ATLAS survey which have a mean M_d/M_* of 2.1×10^{-3}, and have values similar to those of ultra-luminous infrared galaxies (ULIRGs) and high-redshift submillimetre galaxies (SMGs; da Cunha et al. 2010; Rowlands et al. 2014a). Intermediate and older PSBs have M_d/M_* values similar to those of dusty ETGs (Rowlands et al. 2012; Agius et al. 2013), and are higher than those of non-detected ETGs in H-ATLAS. This shows that the older PSBs still harbour a cold ISM. The decrease in dust content with starburst age suggests that the dust in PSBs is being destroyed in the ISM and is no longer balanced by stellar dust production. The similarity of the M_d/M_* of older PSBs and dusty ETGs suggests a possible connection, which should be investigated through further spectroscopic and morphological analyses.

4.3.3 Gas-to-dust ratio

In Fig. 7(c), we show the gas-to-dust ratios (G/D) of the PSBs, as function of starburst age. The PSBs have a large range of G/D, with values of 40–380, with a median of 140. This is similar to the molecular G/D of high metallicity ($12 + \log(O/H) > 8.5$) nearby galaxies in the KINGFISH sample, which have a mean of G/D of 130 (assuming a MW CO to H_2 conversion factor; Rémy-Ruyer et al. 2014). In Fig. 7(c), we observe no significant correlation of G/D with starburst age (Spearman coefficient $\rho = 0.35, \sigma = 0.33$). The weakness of the correlation is largely caused by one source (PSB11). Excluding this source from the correlation analysis results in a Spearman coefficient of 0.72, indicating a significant ($\sigma = 0.03$) positive correlation between G/D and starburst age. Typically the young (<100 Myr) PSBs have low G/D of <100 which is lower than normal spirals, and is more similar to that of high-redshift SMGs (Kovács et al. 2006; Swinbank et al. 2014). The majority of PSBs (>100 Myr) have a molecular G/D consistent with that of normal star-forming galaxies in the nearby Universe.

4.3.4 Chemical evolution models

We now compare our observations to the one-zone chemical evolution models of Morgan & Edmunds (2003) and Rowlands et al. (2014b) to investigate the evolution of the dust and gas in PSBs. By relaxing the instantaneous recycling approximation to account for the lifetimes of stars of different masses, the model tracks the build-up of heavy elements over time produced by low–intermediate mass stars (LIMS) and SNe, where some fraction of the heavy elements will condense into dust. Given an input SFH, gas is converted into stars over time, assuming a Chabrier (2003) initial mass function (IMF). To model the PSBs, we consider a closed-box model, assuming no inflow or outflow of gas or metals. This is justified during the

recent evolution of the PSBs by the observed lack of change in gas-to-stellar mass ratio over time, implying that recent strong outflows are unlikely. The initial gas mass is set at 1.0×10^{10} $M_\odot$, and at the end of the SFH ~ 85 per cent of the total galaxy mass ends up in stars and ~ 15 per cent is in gas, in agreement with our observations. By design, the final stellar masses in the chemical evolution models are in close agreement with the observed stellar masses (mean $M_* = 1 \times 10^{10}$ $M_\odot$) derived from the SED fitting. We adopt a constant SFH of 2 $M_\odot$ yr^{-1} from 0–4.9 Gyr (assuming arbitrarily that our PSBs formed at $z \sim 1$), followed by a starburst of 10 $M_\odot$ yr^{-1} of 100 Myr duration. The starburst produces ~ 10 per cent of the stellar mass in the galaxy, in agreement with observations (Wild et al. 2007, 2009). At $t = 5.0$ Gyr, the SFH is parametrized by an exponentially declining SFR of the form $\exp{-(t/\tau)}$, with $\tau = 300$ Myr, which matches the measured SFRs of the PSBs as a function of starburst age (WHC10).

In Fig. 7(a), the overplotted lines show that the choice of these initial conditions and SFH allow us to match the evolution of the gas-to-stellar mass with starburst age. However, we find that dust produced only by LIMS is not sufficient to match the M_d/M_* and G/D for the young PSBs (thin black line in Figs 7b and c). The large dust masses in these galaxies indicates that rapid dust production (most likely from SNe) is necessary (thick black line). The negative relation between M_d/M_* and starburst age indicates that dust is lost from the system over time, either via outflows or dust destruction by SN shocks or AGN feedback. The closed-box model with no dust destruction results in an almost flat evolution of M_d/M_* with starburst age, regardless of the dust source. We tested that reasonable variations in the assumed SFH of the PSBs are unable to reproduce the observed trends. In order to reproduce the decrease in M_d/M_* with time, we require a model in which moderately strong dust destruction ($m_{ISM} = 500$ $M_\odot$ of ISM cleared of dust per SN explosion) occurs for a short time after the starburst (here assumed to be from 0–100 Myr following the starburst), after which the dust destruction is weaker ($m_{ISM} = 200$ $M_\odot$). We note that when dust destruction is included, our models require very efficient dust production, such that all of the metals produced in SNe are incorporated into dust. This may not be physical, therefore grain growth in the ISM may also play an important role in the dust budget (Rowlands et al. 2014b). We note that dust destruction much stronger than that assumed here, e.g. $m_{ISM} = 1000$ $M_\odot$, as is often assumed in chemical evolution models (Dwek, Galliano & Jones 2007), results in a rapid increase in G/D and a final ratio that is inconsistent with that observed in PSBs older than 100 Myr. One way out of this is to invoke subsequent rapid grain growth in the ISM, but such complex models are not justified by the data presented here.

4.4 Dust temperature

Dust is primarily heated by UV–optical photons from stars, although AGN heating can also contribute in the central regions of massive galaxies (Sauvage & Thuan 1994). Dust then re-radiates the absorbed light in the FIR–submillimetre, with young stars thought to be responsible for heating warm (>60 K) dust (e.g. Sauvage, Vigroux & Thuan 1990; Xu 1990; Popescu et al. 2000; Misiriotis et al. 2001; Bendo et al. 2010). Colder dust is thought to be heated by the diffuse interstellar radiation field (ISRF; Rowan-Robinson & Crawford 1989; Xu & Helou 1996; Stevens, Amure & Gear 2005; Boquien et al. 2011a; Komugi et al. 2011), which originates from photons from old stars (Bendo et al. 2010; Boquien et al. 2011a; Groves et al. 2012) and also young stars where photons leak out of the birth clouds (Kirkpatrick et al. 2014).
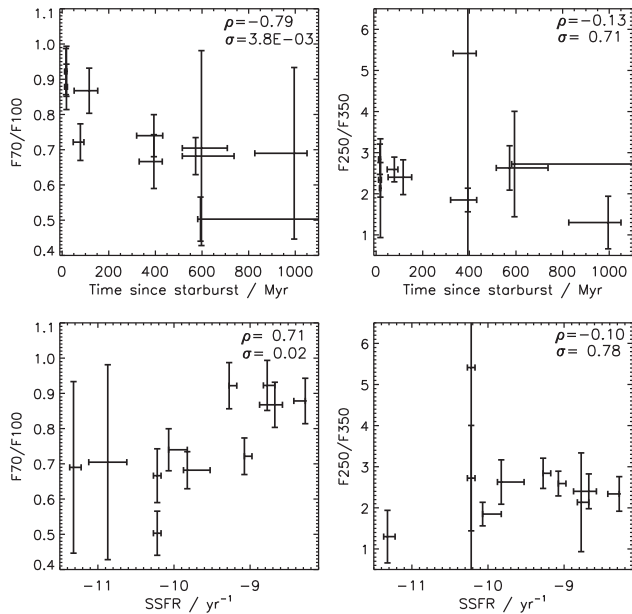
Figure 8. FIR colours $f70/f100$ (warm dust) and $f250/f350$ (R–J slope) as a function of starburst age (upper panels) and SSFR (lower panels). Values in the right of each plot indicate the Spearman rank coefficient (ρ) and the two-sided significance of the deviation of the correlation from zero, or the null hypothesis (σ, a low value indicates a significant correlation). The observed values correspond to a mean effective cold dust temperature dropping from 28 to 17 K, assuming a single modified blackbody fit (see text for further details).

In Fig. 8, we investigate the variation in the effective dust temperature as a function of starburst age. Instead of plotting the model-dependent temperatures output by the MAGPHYS code, we use the colour index $f70/f100$ as a proxy for the presence of warm dust and $f250/f350$ as a proxy for the slope of the R–J tail of the SED. The observed values correspond to a mean effective cold dust temperature of 28 K for the young (<200 Myr) PSBs, dropping to a mean of 17 K for the older (>550 Myr) PSBs, using a single modified blackbody fit to the $\geq 100\,\mu\mathrm{m}$ fluxes (a second component is required to fit warm dust emitting at 70 μm), We assume a dust emissivity $\beta = 2$ and dust mass absorption coefficient $\kappa_{850} = 0.077\,\mathrm{m^2\,kg^{-1}}$. Fitting a two-component modified blackbody to the $\geq 70\,\mu\mathrm{m}$ fluxes leads to the same observed trends. Fixing the warm dust temperature at 45 K (Bourne et al. 2013), the cold dust temperatures from the two-component fit decrease from a mean of 26 to 16 K for the young and old PSBs, respectively. To test if these drops in temperature are significant, we measured the standard deviation of the temperatures for 500 Monte Carlo realizations. We randomly perturbed each of the FIR fluxes by an amount centred on a Gaussian probability distribution of width σ equal to the flux density uncertainty described in Section 3.3. For each realization, we then refit the one- or two-component modified blackbody. The standard deviations of the fitted temperatures for each of the PSBs ranges from 0.5 to 2.2 K (for a one-component modified blackbody), and 0.8 to 2.8 K (for a two-component modified blackbody), which is less than the observed drop in temperature with starburst age.

We therefore conclude that there is a clear trend of decreasing effective dust temperature with increasing time since the starburst ended (Spearman rank coefficient $\rho = -0.79$, $\sigma = 4 \times 10^{-3}$). We find no correlation (Spearman rank coefficient $\rho = -0.13$, $\sigma = 0.71$) between $f250/f350$ and starburst age, indicating that the R–J slope does not change with starburst age.

Since specific SFR (SSFR) decreases over time in our sequence of PSBs, there is also a clear correlation of dust temperature ($f70/f100$) with SSFR (Fig. 8, lower panels; $\rho = 0.71$, $\sigma = 0.02$). We find no correlation between the slope of the R–J side of the SED ($f250/f350$) and SSFR ($\rho = -0.10$, $\sigma = 0.78$). Our results are in agreement with Boquien et al. (2011a) and Boselli et al. (2010, 2012) who found a correlation between birthrate parameter (b, equivalent to SSFR) and effective dust temperature, and no correlation of b with $f250/f350$ in spiral galaxies. Cortese et al. (2014) also found that the effective dust temperature (i.e. the peak of the SED) correlates with SSFR and spatially with young stars (see also Kirkpatrick et al. 2014).

The same trend of dust temperature is also seen in mergers, where the warm dust mass increases with interaction stage (Xilouris et al. 2004; Hwang et al. 2011; Lanz et al. 2013). Local ULIRGs (merger-induced starbursts) are also found to have warmer dust temperatures compared to normal spirals (Clements, Dunne & Eales 2010).

The simplest explanation for the decrease in dust temperature with time since the starburst is that the strength of the ISRF decreases over time as star formation activity in the PSBs declines. This is also observable as a trend with SSFR, because SSFR correlates with the ratio of ionizing (from young stars) to non-ionizing radiation (from old stars) and therefore effectively measures the strength of the ISRF. Dust grains in young PSBs are exposed to a more energetic radiation field from UV emission from young stars, which results in higher dust temperatures. An additional decline in temperature may occur if the dust becomes more diffusely distributed as the PSB ages. Simulations of high-redshift mergers suggest that the increase in dust temperature during a starburst is caused by a combination of the dust being located in a smaller volume, alongside the dust mass decreasing during the starburst (Hayward et al. 2011), allowing the dust to be heated to a higher temperature. However, the decrease in dust mass found in the simulations of starbursts is contrary to our observations, where we find our youngest PSBs to have the highest dust mass fractions. In summary, the decrease in dust temperature is consistent with a decline in the heating contribution from young stars as the PSB ages. We additionally note that there is no evidence of dust heating at late times by an AGN.

4.5 Line ratios

The ratio R21 of 12CO(2–1) to 12CO(1–0) line intensity depends on the optical depth, excitation temperature and spatial distribution[13] of the gas. As our observations consist of one single pointing (with beam sizes of $\sim$22 and $\sim$11 arcsec for 12CO(1–0) and 12CO(2–1), respectively, i.e. a factor of 4 difference in area), we cannot disentangle the effect of gas distribution and physical properties. A value of R21 $\sim$4 indicates that the CO is compact compared to the beam size (Young et al. 2011). Assuming both lines are optically thick and have the same excitation temperature, then R21 $\sim$1 indicates that the CO emission uniformly fills both beams. In Fig. 9, we plot the integrated intensities of the CO(2–1) and CO(1–0) lines (without any aperture corrections) as a function of starburst age. We do not attempt to account for beam dilution as we do not have a good estimate of the size of the CO-emitting region, leading to a large uncertainty in the intrinsic value of R21. We find that most of the PSBs have values of R21 between 1 and 4, suggesting that

---

[13] The measured brightness temperature (a specific intensity) is averaged over the beam area, and so the ratio of the brightness temperatures at different frequencies is determined partly by beam dilution.
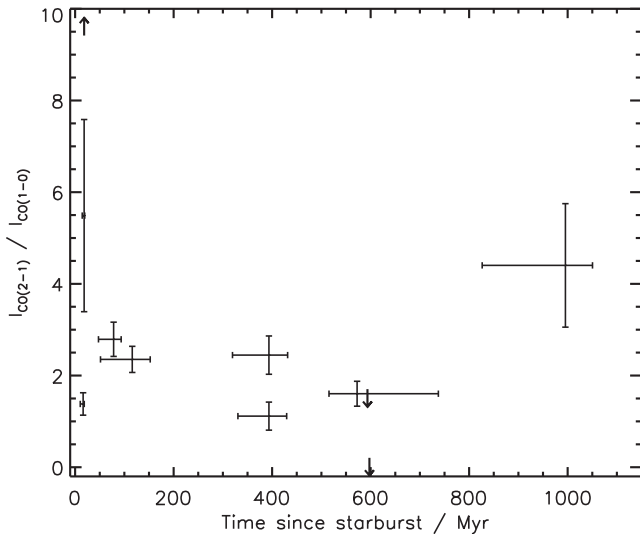
Figure 9. Ratio of the observed 12CO(2–1) to 12CO(1–0) line intensities (no aperture correction applied) as a function of starburst age. The wide range of line ratios indicates that the CO emission does not fill each beam uniformly. There is no trend of line ratio with starburst age.
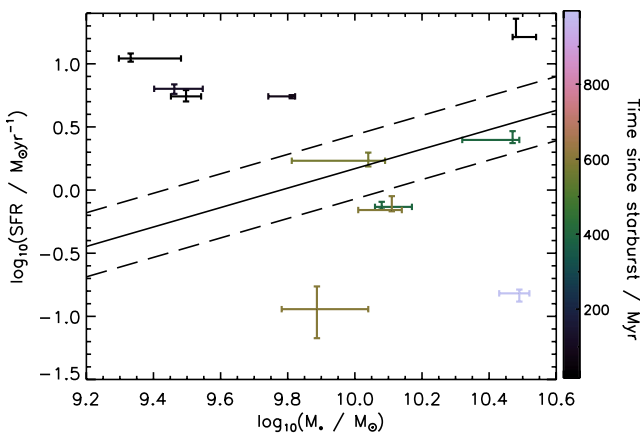

Figure 10. Comparison of the total SFR and the stellar mass of the PSBs (with points colour coded by starburst age) to the median location of blue star-forming galaxies in the local Universe ($0.015 < z < 0.1$) from Elbaz et al. (2007, solid black line). The dashed lines indicate the 68 per cent dispersion in the median of the local relation between SFR and M_*.

the CO does not fill both CO beams uniformly. Furthermore, we do not see a correlation of R21 with starburst age. This indicates that either the distribution and excitation of molecular gas does not vary with starburst age, or that the excitation of the gas is decreasing as the CO distribution becomes more compact. It is likely is that PSBs have a wide range of global excitation conditions, as well as variations within each galaxy. Further investigation of the excitation temperatures of PSBs will require spatially resolved measurements of these sources.

4.6 Where do PSBs lie on the SFR–M_* relation?

Clues to the stellar mass build-up of galaxies can be found via the relatively tight correlation between stellar mass and SFR (e.g. Brinchmann et al. 2004; Daddi et al. 2007; Elbaz et al. 2007; Noeske et al. 2007; Rodighiero et al. 2010; Wuyts et al. 2011; Whitaker et al. 2012b). In Fig. 10, we compare the location of the PSBs to those of

blue star-forming galaxies in the local Universe ($0.015 < z < 0.1$) from Elbaz et al. (2007). The SFRs of the galaxies in Elbaz et al. (2007) were taken from Brinchmann et al. (2004) and utilize the dust-corrected Hα luminosity (corrected to total SFR), and the stellar masses are from Kauffmann et al. (2003a) and use the Bruzual & Charlot (2003) stellar population models. We therefore plot the equivalent observations for the PSBs. The young PSBs lie significantly above the local SFR–M_* relation, with the intermediate-age PSBs coincident with normal star-forming galaxies. Two PSBs lie significantly below the location of blue star-forming galaxies and are consistent with those of $0.02 < z < 0.05$ green valley galaxies (Schawinski et al. 2014).

In the last few years, significant attention has been given to galaxies which lie below the SFR–M_* relation (e.g. Wuyts et al. 2011; Whitaker et al. 2012b; Eales et al., in preparation), which are assumed to be 'quenching' (i.e. switching off their star formation). Given the extra information provided by our detailed SFHs, we have a different picture of where quenching galaxies lie relative to the SFR–M_* relation: galaxies which are 'quenching' can lie on, above and below the location of star-forming galaxies. Furthermore, we have shown in this paper that the older PSBs are not fully 'quenched', with considerable cold gas supplies remaining. The limited information provided by instantaneous SFR and M_* does not give a full picture of the physical mechanisms of quenching. Caution should therefore be exercised when classifying galaxies on the SFR–M_* relation as star-forming galaxies which have remained, and will remain, on the relation for an extended period of time.

4.7 Environment

The large-scale environment of galaxies affects their gas supply. In clusters, the supply of gas can be terminated via interaction of the galaxy ISM with the intracluster medium, which heats or strips gas from the galaxy. In less dense regions such as the field, gas may be readily accreted from the intergalactic medium, although galaxy interactions in small groups can alter gas supplies by triggering a starburst.

We examine the environment of the PSBs in our sample by matching to the SDSS DR7 galaxy group catalogue of Yang et al. (2007). The group catalogue utilizes a halo-based group finder to identify galaxies which reside in the same dark matter halo. We use the group catalogue based on SDSS model magnitudes and redshifts from both SDSS and the 2dF Galaxy Redshift Survey. Halo masses are assigned by rank ordering the groups by stellar mass, although using masses assigned by rank ordering by luminosity would not change our results. We find 10/11 PSBs are identified in the group catalogue, six of which are isolated galaxies, and four PSBs are in groups with 12–59 members. The halo masses of the groups range from $10^{11.9}$ to $10^{14.6}$ M$_\odot$. Our PSBs therefore reside in a variety of galaxy environments, in agreement with previous studies (Dressler & Gunn 1983; Zabludoff et al. 1996; Blake et al. 2004; Quintero et al. 2004; Balogh et al. 2005; Hogg et al. 2006; Poggianti 2009; Yan et al. 2009).

5 DISCUSSION AND CONCLUSIONS

It is often stated in the literature that PSBs could be a channel for the growth of the red sequence, through migration from the blue cloud to the red sequence over a time-scale of 100 Myr to 1 Gyr (Kaviraj et al. 2007; Wild et al. 2009). Transition through the PSB phase potentially represents the fastest 'quenching' mode available to galaxies (Faber et al. 2007; Martin et al. 2007; Barro et al. 2013, 2014; Yesuf et al. 2014), requiring a dramatic starburst event which

can rapidly exhaust gas supplies. Such an event may be triggered by an external interaction or merger, certainly at lower redshifts where gas mass fractions are low. Slower quenching processes may also occur through secular processes (Cortese & Hughes 2009; Fang et al. 2012, 2013; Salim et al. 2012; Schawinski et al. 2014; Eales et al., in preparation), that transfer galaxies through the green valley on longer time-scales. Revealing the existence, and understanding the relative importance, of these two channels for building the red sequence is one of the most important challenges in galaxy evolution.

We have examined the global cold gas, dust and star formation properties of a sample of 11 PSB galaxies which have undergone a central starburst in the last 0–1 Gyr. We derived the physical properties of the PSBs using a multiwavelength data set with optical fibre spectroscopy of the central 3 arcsec, total broad-band photometry from the UV–FIR, and CO measurements which trace the global molecular gas reservoir. As our sample represents some of the most extreme starbursts in massive galaxies in the SDSS volume, we would expect them to experience the fastest quenching of star formation. However, the existence of substantial cold gas reservoirs in all the PSBs studied here suggest that the transition time for local galaxies to become truly 'red and dead' with no possibility for subsequent star formation is ≫1 Gyr, i.e. not particularly fast. The significant cold gas supplies in the recently 'quenched' galaxies, makes it unclear as to whether the galaxies will continue evolving on to the red sequence, or remain in the 'green valley' for an extended period of time (see also French et al. 2015).

AGN feedback is often proposed as a mechanism for fully halting star formation following a starburst (either through gas outflows or heating; e.g. Di Matteo et al. 2005; Croton et al. 2006; Kaviraj et al. 2007; Schawinski et al. 2007, 2009). The lack of change in gas-to-stellar mass ratio with increasing starburst age shows that the bulk of the cold ISM remaining after a starburst is not expelled by stellar winds or AGN feedback. Similarly, the steady decrease in dust temperature indicates that the global ISM is not heated by AGN feedback at later times. For the sample of objects studied in this paper, WHC10 found that the peak in black hole accretion rate occurred ∼250 Myr following the starburst and therefore could not be contributing to the initial rapid decline in star formation observed $\sim 10^7$ yr following the starburst (see also Shin, Strauss & Tojeiro 2011, for radio-loud AGN). In this paper, we show that there is no significant alteration in the physical conditions of the cold ISM that may be attributed to the late-time triggering of an AGN.

Our sample provides a new way to study the alteration in global ISM conditions following a burst of star formation. We observe a steady decline in SFE with starburst age, consistent with a natural decrease in the SFR following consumption of the dense gas reservoir (not traced by our CO observations) by the starburst. A similar steady decrease is observed in the effective dust temperature, which is likely due to a decrease in the ISRF strength as the starburst ages. In the young PSBs, we observe a high dust-to-stellar mass ratio, which declines with increasing starburst age.

Using chemical evolution modelling, we show that rapid and efficient dust production must be important during the starburst, and dust must be formed by both LIMS and SNe in order to match the dust-to-stellar mass ratio and the gas-to-dust mass ratio. The observed decrease of the dust-to-stellar mass ratio with starburst age cannot be modelled only by low rates of dust production due to declining star formation activity. Instead, models must include moderately strong dust destruction due to SN shocks which weakens with starburst age, possibly due to the declining SN rate or changes in density of the ISM.

The gas-to-stellar mass ratio (∼0.2), dust-to-stellar mass ratio (1×10^{-3}) and gas-to-dust mass ratio (100–300) of the oldest PSBs in our sample with ages ∼0.5–1 Gyr are consistent with those of normal spiral galaxies and dust/gas-rich ETGs, and do not resemble those of normal ETGs or red-sequence galaxies. The similarity of the morphology and physical properties (gas-to-stellar mass ratio, dust-to-stellar mass ratio) of the older PSBs to dusty/molecular gas-rich ETGs suggests that these populations may be related, or may have similar endpoints in cold ISM content after a starburst. Further comparisons may reveal that these two populations are intimately linked.

As the central starburst has been identified through 3 arcsec fibre spectroscopy, it is possible that the lack of change in the molecular gas-to-stellar mass ratio may be because the central starburst does not affect the global properties of the galaxy. However, we showed that the global SFR estimated by SED fitting tracks the central SFR as the starburst ages with only a small offset in some objects. It therefore seems unlikely that we will find a significant offset between central and global gas reservoirs. Significant aperture effects certainly do exist in some local SDSS-selected PSBs, for example Pracy et al. (2014) found that star formation is ongoing outside of the PSB core in two very low redshift HI-rich galaxies. It is possible that galaxies that undergo a strong global (rather than central) starburst may be more efficient at completely exhausting or expelling their cold ISM and be a more effective channel by which the red sequence is built. It is also possible that such intense events may be more common at high redshift (Le Borgne et al. 2006; Wild et al. 2009, 2014). Such galaxies can now be selected in large multiwavelength surveys via their UV–near-infrared colours as demonstrated in Wild et al. (2014); these truly global PSBs will be the topic of future investigations.

Recent work on our own Galaxy, the MW, has found that it lies in the 'green valley' (Mutch, Croton & Poole 2011), and its star formation has been roughly constant over the last 3 Gyr (Hernandez, Valls-Gabaud & Gilmore 2000), and perhaps for the last ∼8 Gyr (Haywood et al. 2013; Snaith et al. 2014). A constant SFR suggests that the MW must have been in the green valley for a substantial time (last few Gyr). However, the time resolution of the SFH of the MW is ∼1 Gyr, therefore it is quite possible that bursts of star formation have occurred from time to time, as observed in the objects studied in this paper. It is important to note that despite the status of the MW as a green valley galaxy, it is considered to be unlikely that it is rapidly heading to the red sequence as its gas depletion time is very similar to other local spiral galaxies (Leroy et al. 2013) and to the older PSBs studied here (>300 Myr; Fig. 5). Thus, the MW would fit into a picture where starbursts in local galaxies are followed by a return to pre-disruption normality, although possibly in a slightly earlier-type system, and may lie in the green valley for a few Gyr or longer.

In this paper, we conclude that, while the SFR of PSB galaxies in the local Universe steadily declines with time following the starburst, substantial cold gas reservoirs remain to fuel future star formation, at least up to 0.5–1 Gyr following the starburst. It therefore seems unlikely that massive galaxies in the local Universe which have undergone a strong starburst will contribute to an increase in the number of red-sequence galaxies on even a 1 Gyr time-scale, and they may remain in the 'green valley' for an extended period of time. Morphological analyses of PSB time sequences will help to understand whether the galaxies become increasingly 'early-type' following such starburst episodes. Further observations of the cold ISM in a larger number of older (≳1 Gyr) PSB galaxies are required in order to track their late-time evolution, and reveal whether the

decline in star formation continues and whether they enter the red sequence despite their residual cold gas supplies, perhaps as gas-rich ETGs. Ultimately, studies of galaxies in the local Universe are limited to revealing only what is happening currently. In order to understand the origin of the present-day galaxy bimodality, such observations will have to be repeated at higher redshifts, where present-day red-sequence/elliptical galaxies are forming.

REFERENCES

Abazajian K. N. et al., 2009, ApJS, 182, 543
Agius N. K. et al., 2013, MNRAS, 431, 1929
Alatalo K. et al., 2014, ApJ, 780, 186
Baldry I. K., Glazebrook K., Brinkmann J., Ivezić Ž., Lupton R. H., Nichol R. C., Szalay A. S., 2004, ApJ, 600, 681
Baldwin J. A., Phillips M. M., Terlevich R., 1981, PASP, 93, 5
Balog Z. et al., 2014, Exp. Astron., 37, 129
Balogh M. L., Miller C., Nichol R., Zabludoff A., Goto T., 2005, MNRAS, 360, 587
Barnes J. E., Hernquist L., 1996, ApJ, 471, 115
Barro G. et al., 2013, ApJ, 765, 104
Barro G. et al., 2014, ApJ, 791, 52
Bekki K., Shioya Y., Couch W. J., 2001, ApJ, 547, L17
Bekki K., Couch W. J., Shioya Y., Vazdekis A., 2005, MNRAS, 359, 949
Bell E. F. et al., 2004, ApJ, 608, 752
Bendo G. J. et al., 2010, A&A, 518, L65
Bendo G. J. et al., 2013, MNRAS, 433, 3062
Benson A. J., Bower R. G., Frenk C. S., Lacey C. G., Baugh C. M., Cole S., 2003, ApJ, 599, 38
Bigiel F., Leroy A., Walter F., Brinks E., de Blok W. J. G., Madore B., Thornley M. D., 2008, AJ, 136, 2846
Blake C. et al., 2004, MNRAS, 355, 713
Blanton M. R. et al., 2003, ApJ, 594, 186
Boquien M. et al., 2011a, AJ, 142, 111
Boquien M., Lisenfeld U., Duc P.-A., Braine J., Bournaud F., Brinks E., Charmandaris V., 2011b, A&A, 533, A19
Boselli A. et al., 2010, A&A, 518, L61
Boselli A. et al., 2012, A&A, 540, A54
Boselli A., Cortese L., Boquien M., Boissier S., Catinella B., Lagos C., Saintonge A., 2014, A&A, 564, A66
Bourne N. et al., 2013, MNRAS, 436, 479
Braine J., Combes F., 1993, A&A, 269, 7
Brinchmann J., Charlot S., White S. D. M., Tremonti C., Kauffmann G., Heckman T., Brinkmann J., 2004, MNRAS, 351, 1151
Brown M. J. I. et al., 2009, ApJ, 703, 150
Brown M. J. I. et al., 2014, ApJS, 212, 18
Bruzual G., Charlot S., 2003, MNRAS, 344, 1000
Cappellari M. et al., 2013, MNRAS, 432, 1862
Cardelli J. A., Clayton G. C., Mathis J. S., 1989, ApJ, 345, 245
Casasola V., Bettoni D., Galletta G., 2004, A&A, 422, 941
Chabrier G., 2003, PASP, 115, 763
Ciesla L. et al., 2012, A&A, 543, A161
Clements D. L., Dunne L., Eales S., 2010, MNRAS, 403, 274
Cortese L., Hughes T. M., 2009, MNRAS, 400, 1225
Cortese L. et al., 2014, MNRAS, 440, 942
Couch W. J., Sharples R. M., 1987, MNRAS, 229, 423
Croton D. J. et al., 2006, MNRAS, 365, 11
da Cunha E., Charlot S., Elbaz D., 2008, MNRAS, 388, 1595 (DCE08)
da Cunha E., Charmandaris V., Díaz-Santos T., Armus L., Marshall J. A., Elbaz D., 2010, A&A, 523, A78
Daddi E. et al., 2007, ApJ, 670, 156
Daddi E. et al., 2010, ApJ, 714, L118
Davis T. A. et al., 2014, MNRAS, 444, 3427
Davoust E., Contini T., 2004, A&A, 416, 515
Di Matteo T., Springel V., Hernquist L., 2005, Nature, 433, 604
Downes D., Solomon P. M., 1998, ApJ, 507, 615
Dressler A., Gunn J. E., 1983, ApJ, 270, 7
Dressler A., Oemler A., Jr, Poggianti B. M., Gladders M. D., Abramson L., Vulcani B., 2013, ApJ, 770, 62
Dunne L., Eales S., Edmunds M., Ivison R., Alexander P., Clements D. L., 2000, MNRAS, 315, 115
Dwek E., Galliano F., Jones A. P., 2007, ApJ, 662, 927
Elbaz D. et al., 2007, A&A, 468, 33
Faber S. M. et al., 2007, ApJ, 665, 265
Falkenberg M. A., Kotulla R., Fritze U., 2009, MNRAS, 397, 1940
Fang J. J., Faber S. M., Salim S., Graves G. J., Rich R. M., 2012, ApJ, 761, 23
Fang J. J., Faber S. M., Koo D. C., Dekel A., 2013, ApJ, 776, 63
French K. D., Yang Y., Zabludoff A., Narayanan D., Shirley Y., Walter F., Smith J.-D., Tremonti C. A., 2015, ApJ, preprint (arXiv:1501.00983)
Gao Y., Solomon P. M., 2004, ApJ, 606, 271
García-Burillo S., Usero A., Alonso-Herrero A., Graciá-Carpio J., Pereira-Santaella M., Colina L., Planesas P., Arribas S., 2012, A&A, 539, A8
Genzel R. et al., 2010, MNRAS, 407, 2091
Georgakakis A. et al., 2008, MNRAS, 385, 2049
Goto T., 2005, MNRAS, 357, 937
Goto T., 2007, MNRAS, 381, 187
Goto T. et al., 2003, PASJ, 55, 771
Griffin M. J. et al., 2010, A&A, 518, L3
Groves B. et al., 2012, MNRAS, 426, 892
Haynes M. P. et al., 2011, AJ, 142, 170
Hayward C. C., Kereš D., Jonsson P., Narayanan D., Cox T. J., Hernquist L., 2011, ApJ, 743, 159
Haywood M., Di Matteo P., Lehnert M. D., Katz D., Gómez A., 2013, A&A, 560, A109

Hernandez X., Valls-Gabaud D., Gilmore G., 2000, MNRAS, 316, 605
Hogg D. W., Masjedi M., Berlind A. A., Blanton M. R., Quintero A. D., Brinkmann J., 2006, ApJ, 650, 763
Hopkins P. F., Bundy K., Hernquist L., Ellis R. S., 2007, ApJ, 659, 976
Huang M.-L., Kauffmann G., 2014, MNRAS, 443, 1329
Hwang H. S. et al., 2011, A&A, 535, A60
Jarrett T. H., Chester T., Cutri R., Schneider S., Skrutskie M., Huchra J. P., 2000, AJ, 119, 2498
Jarrett T. H. et al., 2012, AJ, 144, 68
Kauffmann G. et al., 2003a, MNRAS, 341, 33
Kauffmann G. et al., 2003b, MNRAS, 346, 1055
Kaviraj S., Kirkby L. A., Silk J., Sarzi M., 2007, MNRAS, 382, 960
Kaviraj S., Schawinski K., Silk J., Shabala S. S., 2011, MNRAS, 415, 3798
Kennicutt R. C., Jr, 1998, ApJ, 498, 541 (K98)
Kewley L. J., Dopita M. A., Sutherland R. S., Heisler C. A., Trevena J., 2001, ApJ, 556, 121
Khalatyan A., Cattaneo A., Schramm M., Gottlöber S., Steinmetz M., Wisotzki L., 2008, MNRAS, 387, 13
Kirkpatrick A. et al., 2014, ApJ, 789, 130
Komugi S. et al., 2011, PASJ, 63, 1139
Kovács A., Chapman S. C., Dowell C. D., Blain A. W., Ivison R. J., Smail I., Phillips T. G., 2006, ApJ, 650, 592
Landsman W. B., 1993, in Hanisch R. J., Brissenden R. J. V., Barnes J., eds, ASP Conf. Ser. Vol. 52, Astronomical Data Analysis Software and Systems II. Astron. Soc. Pac., San Francisco, p. 246
Lanz L. et al., 2013, ApJ, 768, 90
Le Borgne D. et al., 2006, ApJ, 642, 48
Lehnert M. D., Heckman T. M., 1996, ApJ, 472, 546
Leroy A., Bolatto A., Walter F., Blitz L., 2006, ApJ, 643, 825
Leroy A. K., Walter F., Brinks E., Bigiel F., de Blok W. J. G., Madore B., Thornley M. D., 2008, AJ, 136, 2782
Leroy A. K. et al., 2013, AJ, 146, 19
Levesque E. M., Kewley L. J., Larson K. L., 2010, AJ, 139, 712
Lisenfeld U. et al., 2011, A&A, 534, A102
Martin D. C. et al., 2007, ApJS, 173, 342
Mendel J. T., Simard L., Ellison S. L., Patton D. R., 2013, MNRAS, 429, 2212
Mihos J. C., Hernquist L., 1994, ApJ, 431, L9
Mihos J. C., Hernquist L., 1996, ApJ, 464, 641
Misiriotis A., Popescu C. C., Tuffs R., Kylafis N. D., 2001, A&A, 372, 775
Morgan H. L., Edmunds M. G., 2003, MNRAS, 343, 427
Moshir M., 1989, IRAS Faint Source Survey, Explanatory Supplement Sersion 1 and Tape. Infrared Processing and Analysis Center, California Institute of Technology, Pasadena, CA
Mutch S. J., Croton D. J., Poole G. B., 2011, ApJ, 736, 84
Nguyen H. T. et al., 2010, A&A, 518, L5
Noeske K. G. et al., 2007, ApJ, 660, L43
Ott S., 2010, in Mizumoto Y., Morita K.-I., Ohishi M., eds, ASP Conf. Ser. Vol. 434, Astronomical Data Analysis Software and Systems XIX. Astron. Soc. Pac., San Francisco, p. 139
Pilbratt G. L. et al., 2010, A&A, 518, L1
Poggianti B. M. O., 2009, ApJ, 693, 112
Poglitsch A. et al., 2010, A&A, 518, L2
Popescu C. C., Misiriotis A., Kylafis N. D., Tuffs R. J., Fischera J., 2000, A&A, 362, 138
Pracy M. B., Kuntschner H., Couch W. J., Blake C., Bekki K., Briggs F., 2009, MNRAS, 396, 1349
Pracy M. B., Owers M. S., Zwaan M., Couch W., Kuntschner H., Croom S. M., Sadler E. M., 2014, MNRAS, 443, 388
Quintero A. D. et al., 2004, ApJ, 602, 190
Rémy-Ruyer A. et al., 2014, A&A, 563, A31
Rodighiero G. et al., 2010, A&A, 518, L25
Roussel H., 2013, PASP, 125, 1126
Rowan-Robinson M., Crawford J., 1989, MNRAS, 238, 523
Rowlands K. et al., 2012, MNRAS, 419, 2545
Rowlands K. et al., 2014a, MNRAS, 441, 1017
Rowlands K., Gomez H. L., Dunne L., Aragón-Salamanca A., Dye S., Maddox S., da Cunha E., Werf P. v. d., 2014b, MNRAS, 441, 1040

Sage L. J., Welch G. A., Young L. M., 2007, ApJ, 657, 232
Saintonge A. et al., 2011a, MNRAS, 415, 32
Saintonge A. et al., 2011b, MNRAS, 415, 61
Salim S., Fang J. J., Rich R. M., Faber S. M., Thilker D. A., 2012, ApJ, 755, 105
Sanders D. B., Mirabel I. F., 1996, ARA&A, 34, 749
Sanders D. B., Scoville N. Z., Soifer B. T., 1991, ApJ, 370, 158
Sauvage M., Thuan T. X., 1994, ApJ, 429, 153
Sauvage M., Vigroux L., Thuan T. X., 1990, A&A, 237, 296
Schawinski K., Thomas D., Sarzi M., Maraston C., Kaviraj S., Joo S.-J., Yi S. K., Silk J., 2007, MNRAS, 382, 1415
Schawinski K. et al., 2009, ApJ, 690, 1672
Schawinski K. et al., 2014, MNRAS, 440, 889
Schlegel D. J., Finkbeiner D. P., Davis M., 1998, ApJ, 500, 525
Shin M.-S., Strauss M. A., Tojeiro R., 2011, MNRAS, 410, 1583
Skrutskie M. F. et al., 2006, AJ, 131, 1163
Smith D. J. B. et al., 2012, MNRAS, 427, 703
Smith D. J. B. et al., 2013, MNRAS, 436, 2435
Snaith O. N., Haywood M., Di Matteo P., Lehnert M. D., Combes F., Katz D., Gómez A., 2014, ApJ, 781, L31
Snyder G. F., Cox T. J., Hayward C. C., Hernquist L., Jonsson P., 2011, ApJ, 741, 77
Solomon P. M., Vanden Bout P. A., 2005, ARA&A, 43, 677
Solomon P. M., Downes D., Radford S. J. E., Barrett J. W., 1997, ApJ, 478, 144
Springel V., Di Matteo T., Hernquist L., 2005, ApJ, 620, L79
Stark D. V., Kannappan S. J., Wei L. H., Baker A. J., Leroy A. K., Eckert K. D., Vogel S. N., 2013, ApJ, 769, 82
Stevens J. A., Amure M., Gear W. K., 2005, MNRAS, 357, 361
Strateva I. et al., 2001, AJ, 122, 1861
Swinbank A. M. et al., 2014, MNRAS, 438, 1267
Tacconi L. J. et al., 2008, ApJ, 680, 246
Tremonti C. A. et al., 2004, ApJ, 613, 898
Veilleux S., Osterbrock D. E., 1987, ApJS, 63, 295
Whitaker K. E., Kriek M., van Dokkum P. G., Bezanson R., Brammer G., Franx M., Labbé I., 2012a, ApJ, 745, 179
Whitaker K. E., van Dokkum P. G., Brammer G., Franx M., 2012b, ApJ, 754, L29
Wild V., Kauffmann G., Heckman T., Charlot S., Lemson G., Brinchmann J., Reichard T., Pasquali A., 2007, MNRAS, 381, 543
Wild V., Walcher C. J., Johansson P. H., Tresse L., Charlot S., Pollo A., Le Fèvre O., de Ravel L., 2009, MNRAS, 395, 144
Wild V., Heckman T., Charlot S., 2010, MNRAS, 405, 933 (WHC10)
Wild V. et al., 2014, MNRAS, 440, 1880
Wong O. I. et al., 2006, MNRAS, 371, 1855
Wong O. I., Webster R. L., Kilborn V. A., Waugh M., Staveley-Smith L., 2009, MNRAS, 399, 2264
Wong O. I. et al., 2012, MNRAS, 420, 1684
Wright E. L. et al., 2010, AJ, 140, 1868
Wuyts S. et al., 2011, ApJ, 742, 96
Xilouris E. M., Georgakakis A. E., Misiriotis A., Charmandaris V., 2004, MNRAS, 355, 57
Xu C., 1990, ApJ, 365, L47
Xu C., Helou G., 1996, ApJ, 456, 163
Yan R., Newman J. A., Faber S. M., Konidaris N., Koo D., Davis M., 2006, ApJ, 648, 281
Yan R. et al., 2009, MNRAS, 398, 735
Yang X., Mo H. J., van den Bosch F. C., Pasquali A., Li C., Barden M., 2007, ApJ, 671, 153
Yang Y., Zabludoff A. I., Zaritsky D., Mihos J. C., 2008, ApJ, 688, 945
Yates R. M., Kauffmann G., 2014, MNRAS, 439, 3817
Yesuf H. M., Faber S. M., Trump J. R., Koo D. C., Fang J. J., Liu F. S., Wild V., Hayward C. C., 2014, ApJ, 792, 84
York D. G. et al., 2000, AJ, 120, 1579
Young J. S., Kenney J. D., Tacconi L., Claussen M. J., Huang Y.-L., Tacconi-Garman L., Xie S., Schloerb F. P., 1986, ApJ, 311, L17
Young L. M. et al., 2011, MNRAS, 414, 940

Zabludoff A. I., Zaritsky D., Lin H., Tucker D., Hashimoto Y., Shectman
S. A., Oemler A., Kirshner R. P., 1996, ApJ, 466, 104
Zwaan M. A., Kuntschner H., Pracy M. B., Couch W. J., 2013, MNRAS,
432, 492

APPENDIX A: PSB GALAXY SELECTION

Samples of PSB galaxies are traditionally selected to lack emission
lines which trace star formation (e.g. Hα, [O II]), and exhibit deep

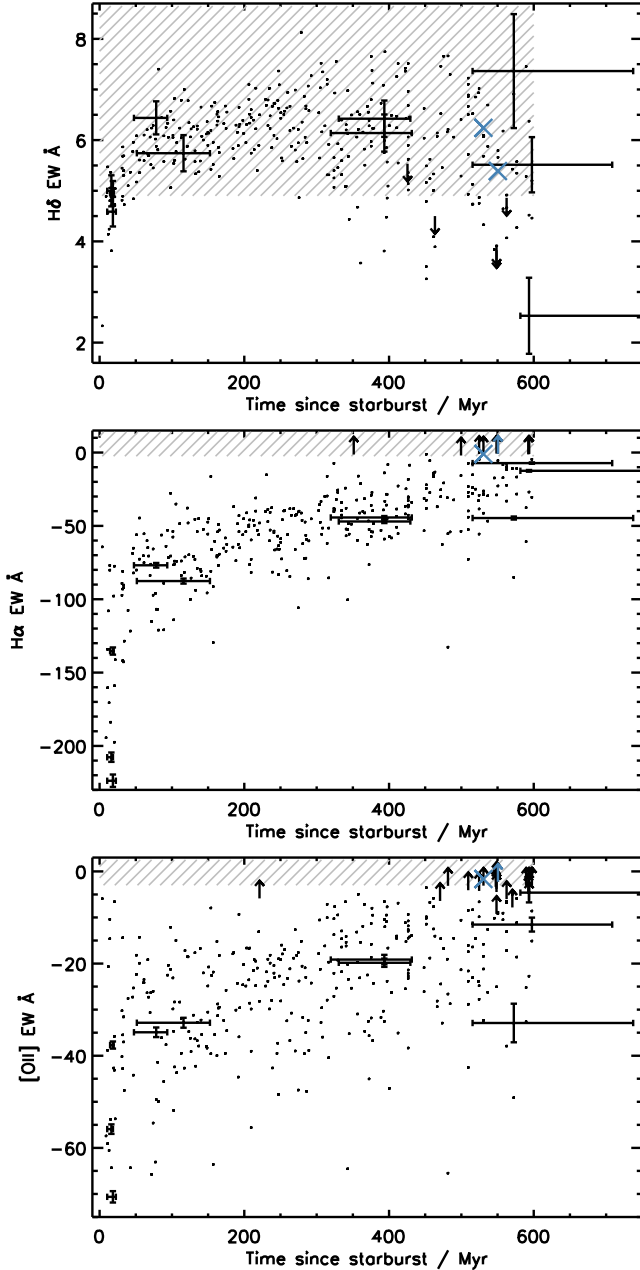**Figure A1.** EWs of the $H\delta_A$, Hα and [O II] emission lines as a function of
starburst age for the SDSS bulge-dominated PSB parent sample (dots) and
the 11 PSBs studied in this paper (thick points with error bars). The grey
areas denote the equivalent width at which a galaxy would be identified
as a PSB galaxy by Goto et al. (2003). The blue crosses indicate galaxies
which meet all three criteria required by Goto et al. (2003) to be classified
as a PSB. Upper limits at the 3σ level are shown for galaxies with SNR<3,
sources with blue upper limits have SNR<3 in either Hα or [O II] EW and
meet the Goto et al. (2003) criteria at the 3σ level.

Balmer absorption lines which signify a dominant A/F stellar popu-
lation. We briefly examine which of our PSBs selected via our PCA
technique would be selected as PSBs using the criteria of Goto et al.
(2003), Goto (2005, 2007), who require Hα equivalent width (EW)
>-2.5 Å, Hδ EW >5 Å, [O II] EW >-3 Å (where absorption is
positive EW and emission is negative EW).

In Fig. A1, we show the line EWs as a function of starburst
age for the 11 PSBs studied in this sample and the SDSS bulge-
dominated PSB parent sample. The line EWs are from the MPA-
JHU catalogue.[14] Of the 11 PSBs studied in this paper, none would
meet the Goto et al. (2003) criteria due to the presence of Hα and
[O II] emission. Of the parent sample of PSBs with starburst age
<600 Myr and measurements of all three lines, only 5/377 meet the
criteria, although four of these sources have SNR <3 in either Hα
or [O II] EW.[15] Of these four sources, only one PSB meets the Goto
et al. (2003) criteria at the 3σ level. It can be seen from Fig. A1
that selection criteria requiring no emission only select PSBs with
ages older than 400 Myr. This is primarily due to the relatively
slow decline in SFR following a starburst, although additionally it
excludes all narrow-line AGN which are more prevalent in PSBs
than other galaxies (Yan et al. 2006; Wild et al. 2010). Samples
where an emission line cut has been applied cannot be used to study
the evolution of starbursts into PSBs.

APPENDIX B: SPECTRA AND IMAGES
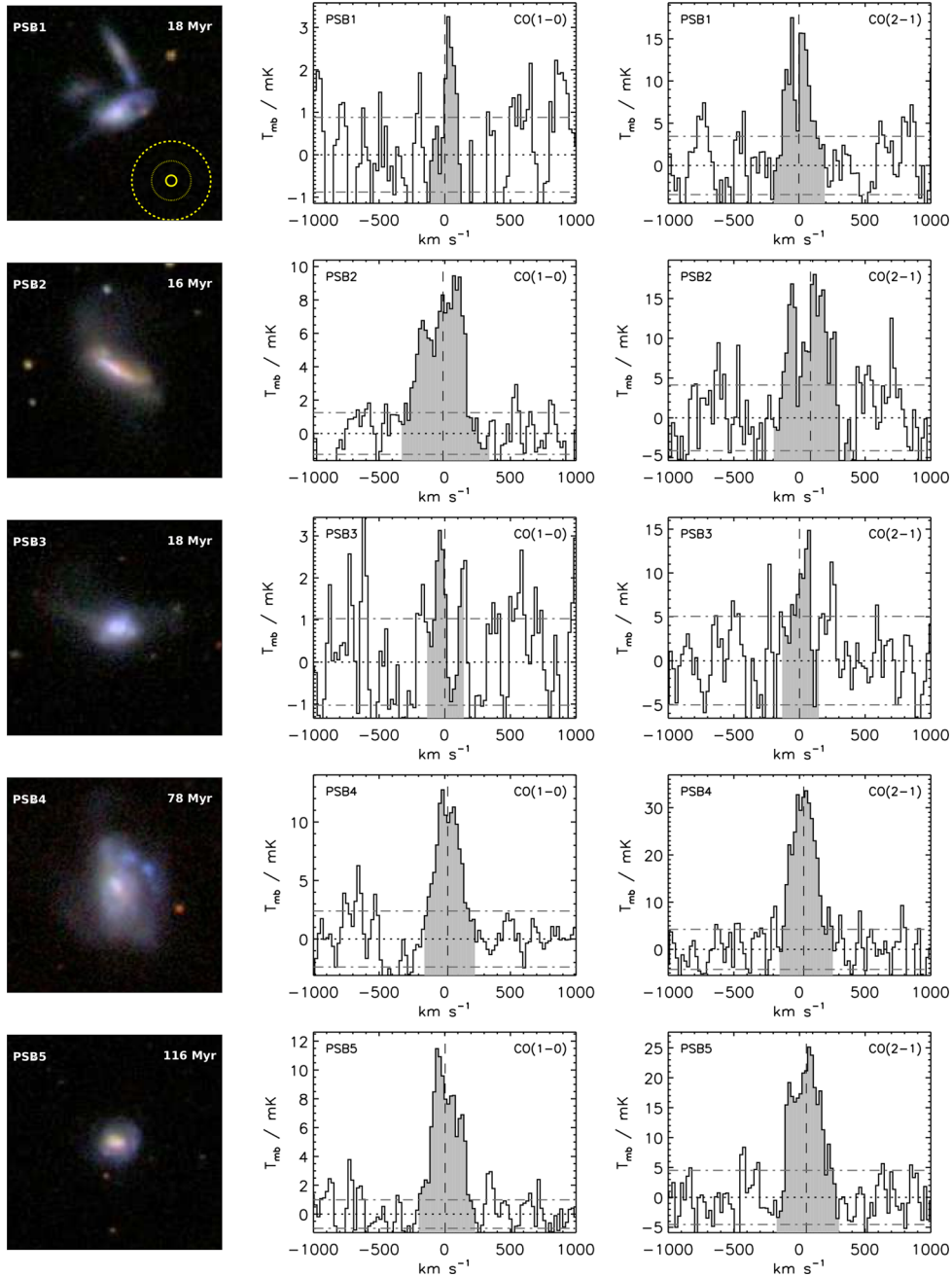
APPENDIX C: SED FITS

Figure B1. Left: SDSS *gri* cutouts of the PSBs, cutouts are 60 arcsec on a side. In the first image, we show the extent of the 3 arcsec SDSS fibre (solid), the CO(1–0) beam (dashed) and the CO(2–1) beam (dotted). The CO ^{12}CO(1–0) (centre) and ^{12}CO(2–1) (right) spectra in units of main beam brightness temperature for the PSBs. The *x*-axis indicates the velocity offset of the line corrected to the systemic velocity of the galaxy from optical spectra. The raw CO(1–0) and CO(2–1) data have been smoothed with a boxcar of 10 and 15 velocity resolution elements, respectively, and binned to $21\,\mathrm{km\,s^{-1}}$. The grey shaded area indicates the CO line, and the dashed lines indicate the 3σ scatter around the baseline.
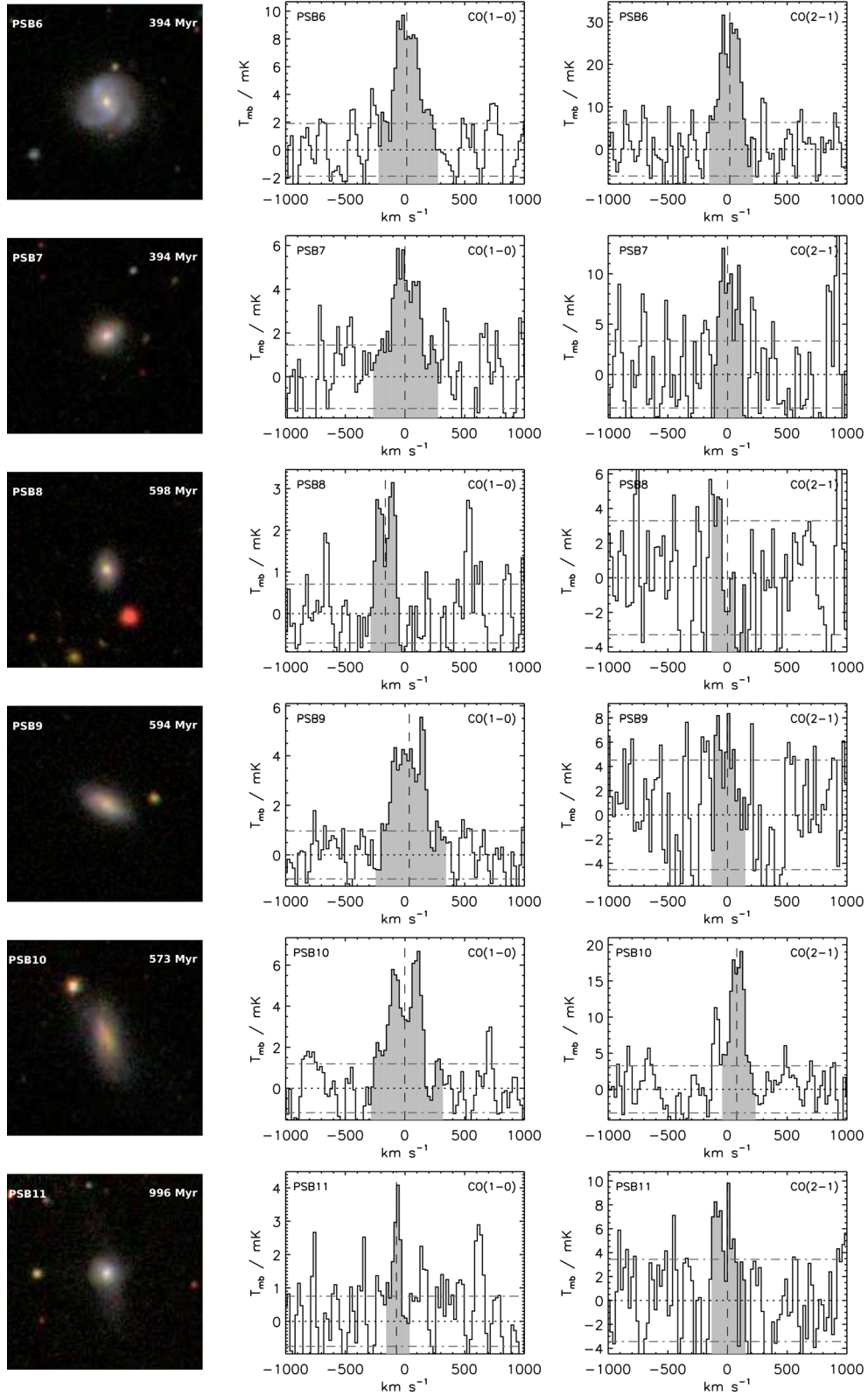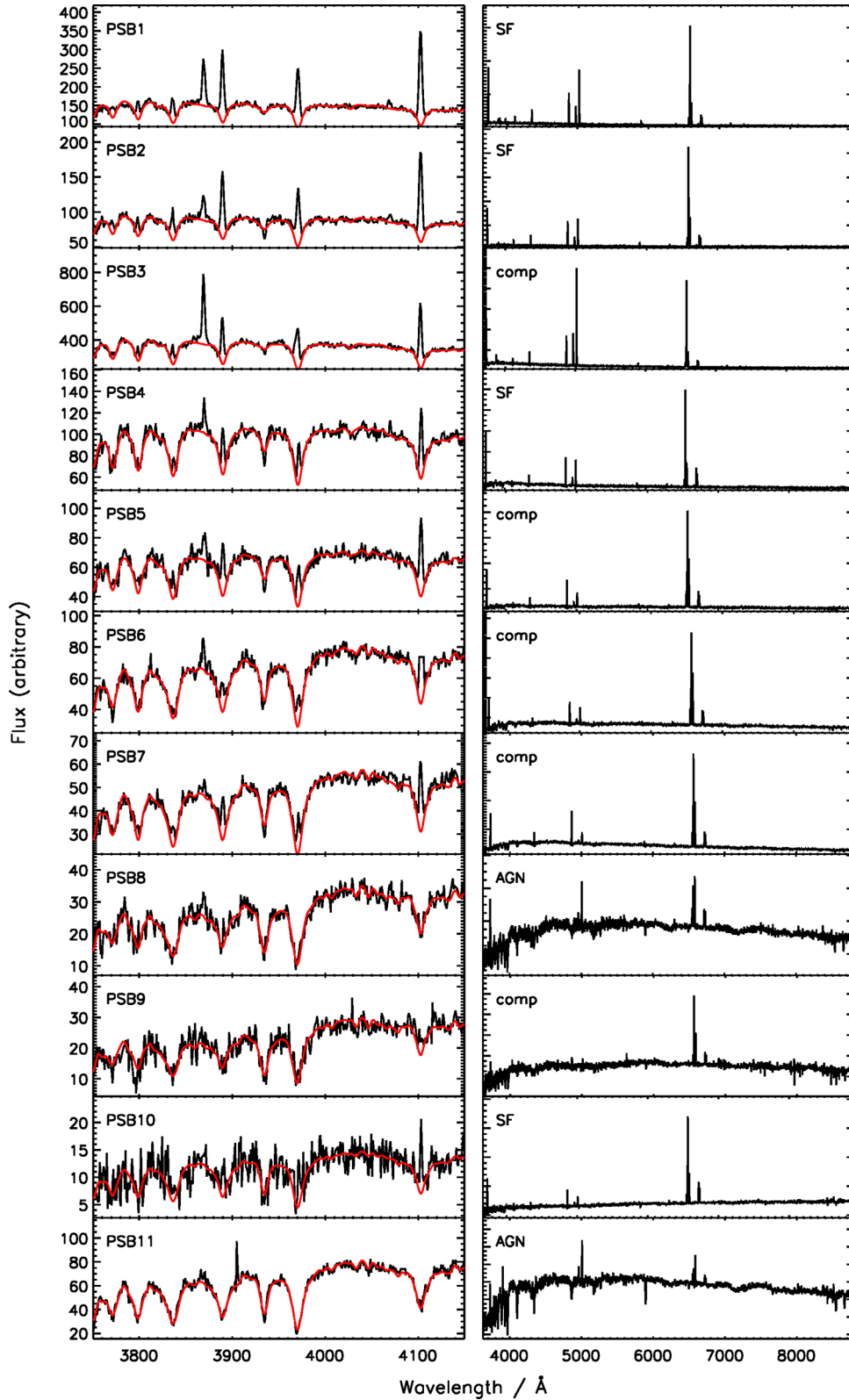
Figure B1. *continued*

Figure B2. The optical spectra of the 11 PSBs. The left-hand panel shows the 4000 Å break region in detail, with the fitted eigenspectra overplotted in red (the emission lines are masked during the fitting). The right-hand panel shows the full extent of the SDSS spectra. The spectra are ordered by starburst age: $<20\,\mathrm{Myr}$ (PSB1, 2, 3), $\sim 100\,\mathrm{Myr}$ (PSB4 and 5), $\sim 400\,\mathrm{Myr}$ (PSB6, 7), $\sim 600\,\mathrm{Myr}$ (PSB8, 9 and 10) and $\sim 1\,\mathrm{Gyr}$ (PSB11).
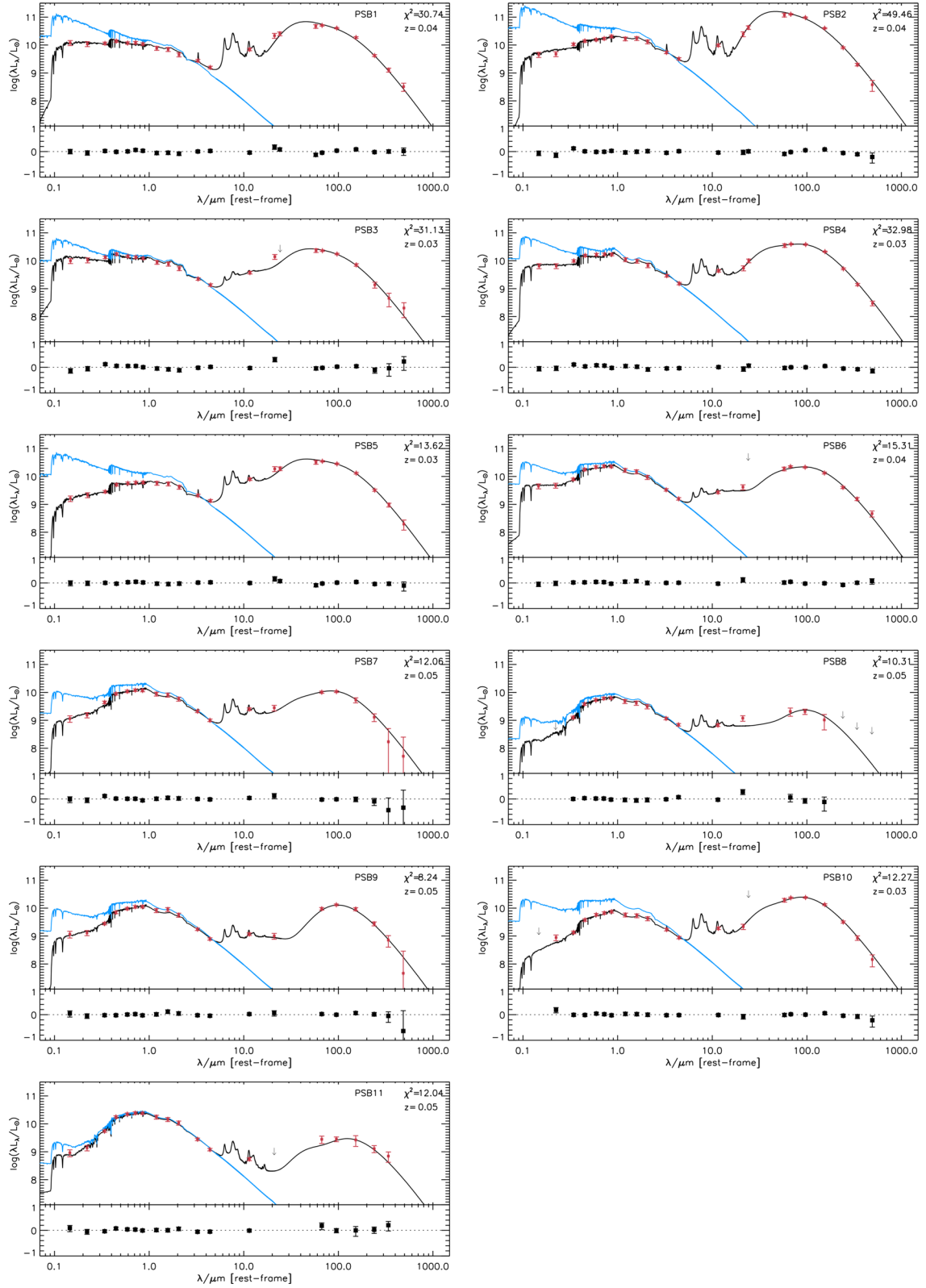
Figure C1. Multiwavelength SEDs of the 11 PSBs in our sample, with observed photometry (red points) from the rest-frame UV to the submillimetre. Upper limits are shown as arrows, and errors on the photometry are described in Section 3. The solid black line is the best-fitting model SED and the solid blue line is the unattenuated optical model. The residuals of the fit are shown in the panel below each SED.

This paper has been typeset from a TEX/LATEX file prepared by the author.